Icarus 388 (2022) 115231

Contents lists available at ScienceDirect

Icarus

journal homepage: www.elsevier.com/locate/icarus

Characteristics of de Gerlache crater, site of girlands and slope exposed ice in a lunar polar depression

A. Kereszturi [a,f,*], R. Tomka [a,b,f], P.A. Gläser [c], B.D. Pal [a,f], V. Steinmann [a,d,f], T. Warren [e]

[a] Konkoly Thege Miklos Astronomical Institute, Budapest, Hungary, Research Centre for Astronomy and Earth Sciences, Hungary
[b] Geographical Institute, Research Centre for Astronomy and Earth Sciences, Hungary
[c] Technische Universität Berlin, Department of Planetary Geodesy, Berlin, Germany
[d] Eotvos Lorand University of Sciences, Department of Physical Geography, Hungary
[e] Atmospheric, Oceanic and Planetary Physics Department, University of Oxford, Oxford, United Kingdom
[f] CSFK, MTA Centre of Excellence, Budapest, Konkoly Thege Miklós út 15-17., H-1121, Hungary

ARTICLE INFO

Keywords:
Moon
Polar ice
DeGerlache crater

ABSTRACT

The 31 km diameter and 7.5 km deep de Gerlache crater, located 30 km from the southern pole of the Moon was surveyed. At its bottom a 15 km diameter younger crater can be also found beside many smaller overprinting craters. At moderately sloping terrains a few m high, 100–200 m wide, curving quasi-parallel, km long set of ridges could be identified, which seem to be widespread on the surface, and might cover the half or even more of the crater. We named these "girland like features" in this work, which seem to be produced by mass movements on slopes (however differ from most of the already identified slope features, which show downslope elongated lineaments or fallen/redeposited debris on the Moon). At all locations they are superposed by recently formed 10–50 m diameter craters, thus might be older than the equilibrium crater population shown age of about 100 Ma old. This is the first identification of these features at the polar terrains, where they might contribute both in the shielding or exposing of subsurface ice. In de Gerlache crater ice occurrences have previously been located on moderately steep slopes, indicating they might be exposed by mass movement processes, where active movements might have happened in the last some 10 Ma using crater statistics based age of the shallow regolith layer. Only half of them were located at areas with modelled surface temperatures below 110 K, where temperature might be not enough to keep most of the deposited H_2O there on Ga time scale. However the real values are probably more diverse because of the limited spatial resolution of available temperature data. Target areas are indicated for possible future missions, where periodic solar illumination, and subsurface ice at 0.5 m depth could be also present.

1. Introduction

This work aims to analyze a polar crater at the southern hemisphere of the Moon: the de Gerlache crater that possibly hosts water ice with specfic focus on surface features and their possible relation to ice there. This crater is located at −88.6° 260°, about 30 km to the north of the polar situated Shackleton crater. It has 31 km diameter and depth of roughly 7.5 km. It is almost 50% larger than Shackleton, and shows more degraded crater rim crest than it. De Gerlache crater may host water ice occurrence (see later results by Fisher et al., 2017, Li et al., 2018) and is hiding in permanent shadow (Mazarico et al., 2011), however some parts of its southern interior slope are occasionally illuminated. Understanding the connection between topographic features and WAC and NAC image based appearance at illuminated regions, helps to interpret only topographic data at permanently shadowed locations without optical images. The main questions in this work are: What types of surface processes influence the regolith and possible ice in it? What do these results indicate surface features regarding the origin and occurrence of ice there? What characteristics are preferable that make de Gerlache crater as a target for future lander mission on the Moon?

In the first part of this paper a short summary is presented on the importance of southern polar craters, then the used methods are described. In the Results section the morphological, topographical, age and ice occurrence related results are presented. In the Discussion section the possible origin of these features (including girlands, craters, and

---

* Corresponding author at: Konkoly Thege Miklos Astronomical Institute, Budapest, Hungary, Research Centre for Astronomy and Earth Sciences, Hungary.
E-mail address: kereszturi.akos@csfk.org (A. Kereszturi).

https://doi.org/10.1016/j.icarus.2022.115231
Received 8 September 2021; Received in revised form 14 August 2022; Accepted 15 August 2022

slope features), their context and location in the lunar history are overviewed, and finally the crater as a possible future mission target is summarized.

1.1. Background information

Importance of lunar volatiles is related partly to the general aspects of volatiles on planetary bodies as they are indicators of planetary evolution (Gillmann et al., 2021; Tartèse et al., 2021), also important for mission planning (Austin et al., 2020), in-situ resource utilization (Trigo-Rodríguez et al., 2020), and could support future manned activity there (Spudis et al., 2010). However there is a serious knowledge gap in this topic (Jawin et al., 2019), that should be targeted by further research activity. The current ice distribution on the Moon might indicate past ice deposition episodes, when the spin axis location differed from the current one (Siegler et al., 2015, 2016), thus ice may have relevance for the geological history. Current activity, like ongoing meteorite gardening, solar wind implementation, regolith movement probably also have signatures in ice distribution, including input, transport and stability of ice, as well as impact events, various regolith migration (Grant and Schultz, 1991) and resurfacing processes (Cocks et al., 2002).

Various **observations show there are trapped volatiles**, including H_2O, at the polar regions of the Moon. The importance of the permanently shadowed regions (PSRs) on cold trapping of volatiles was published in the early 1970s (Arnold, 1979), and recent observations demonstrated their probable existence. Ultraviolet Lyman-alpha (LAMP) spectroscopic observations of lunar polar regions suggested the presence of ice in patchy distribution (Hayne et al., 2015a, 2015b), just like the 1.064-nm laser reflectance measurements collected by the Lunar Orbiter Laser Altimeter (LOLA) (Fisher et al., 2017) indicated elevated albedo in the area of the PSR. This is compatible with the presence of ice, however other factors also should be considered like the decreased space weathering there (Zuber et al., 2012), and contribution from other volatile species like sulphur-bearing materials, carbon-dioxide or hydrocarbons, which may also contribute or even dominate. Constant and very low temperatures in PSRs could also decrease the mechanical fragmentation of boulders, possibly influencing the darkening of the lunar surface (Qiao et al., 2019). A further possibility is that exposure of less mature materials by downslope mass movements happen on slopes (up to ~25°) also increasing the albedo (Haruyama et al., 2008). The infrared spectroscopy of Moon Mineralogy Mapper (M3) instrument (Li et al., 2018) and neutron spectroscopy (Teodoro et al., 2014) also confirmed the existence of ice. However hydrogen concentrations do not show uniform enhancement within PSRs (Elphic et al., 2007), and also do correlate strongly with locations of volatile stability based on temperature as expected (Mitrofanov et al., 2010). The LCROSS observation of the ejecta from Cabeus crater after the artificial impact indicated 5.6 ± 0.4% volatiles in the regolith (Colaprete et al., 2010).

Craters both on Mercury and the Moon are important targets in general, not only as they may host ice (Chabot et al., 2018; Neumann et al., 2013; D'Incecco et al., 2015), but also as a site to accumulate various volatile materials inside them (Fastook et al., 2019; Chabot et al., 2013, 2014). Earth based radar analysis of Shackleton crater (Zuber et al., 2012; Stacy et al., 1997) indicated dm thick or even thinner ice or ice embedded material between grains. Model simulations supported the probable existence of volatiles and especially water ice in the polar regions (Paige et al., 2010) with that around 15% of the southern polar area of latitude <80° might hold water ice, especially if buried by several cm thick dusty layer. Altogether PSRs cover 26,000–30,000 km^2 at both poles of the Moon, larger at the southern hemisphere (Crawford, 2015) with potential micro-cold traps about 40,000 km^2 above 65° latitude (Hayne et al., 2021); because of the 1.5° tilt of rotational axis.

The most of the ice tend to be hosted by old craters >3.8 Ga, although the larger craters with more shadowing capability usually in bigger and older (Deutsch et al., 2020). However it is not well known what causes the patchy distribution, as might be related to age, impact related burial and exposure processes, and even further influenced by true polar wander of the Moon (Siegler et al., 2016) influencing the stability regardless the source of ice.

Among the several ice formation and delivery models, the **impact driven H_2O input** is one of the most popular scenario (Prem et al., 2015), where part of the delivered H_2O after the impact explosion of comets (Klumov and Berezhnoi, 2002; Shevchenko, 1999) is trapped in the cold polar locations. Ephemeral **volcanic activity** might also produce such a lunar atmosphere, which could survive in the order of 10 Ma (Needham and Kring, 2017) and could be partly cold-trapped at polar regions after migration in the collision based ephemeral lunar atmosphere. However this might be realistic only under exceptional cases (Head et al., 2020). Another model is that solar wind implantation produced reduced Fe^{2+} supports the formation of hydroxide and might produce water in the gas phase in the lunar regolith (Arnold, 1979) based on the Apollo samples, and related new laboratory simulation confirmed the production by H implantation in silicates (Zhu et al., 2019).

2. Methods

During the research work the following types of activities were done: 1. Morphological analysis of the de Gerlache carter using images and topographic dataset, with the evaluation of slopes, their surface morphology and small overprinting craters there. 2. Correlation of observed and predicted ice occurrences identified by other authors (see the M3 and LOLA based observations in the Introduction) and surface features found in this work. 3. Joint evaluation of various ice occurrence types and surface characteristics focusing on topography and morphology. 4. Estimation of mission relevant aspects of ice analysis there.

For the survey and evaluation of surface morphology, **WAC and NAC images** were analyzed. These images were recorded by the Lunar Reconnaissance Orbiter Camera (LROC), onboard NASA's Lunar Reconnaissance Orbiter (LRO) spacecraft (Chin et al., 2007; Tooley et al., 2010). The LROC detector captures high resolution black and white images of the Moon, by the Wide Angle Camera (WAC) with 100 m/px resolution in seven color bands (Humm et al., 2016), and panchromatic Narrow Angle Camera (NAC) images with 0.5 m/px resolution of a 5 km swath. For NAC images a two steps approaches was applied: the searching for potential images was done by JMARS software, where the candidate images could be rendered moderately fast, thus several 100 of them could be evaluated as a first approach in 1–2 days. After selecting the best images (Table 1), georeferencing was done in ArcGIS (in the first phase by the label files, however in a second phase manual improvement was necessary), using IAU Moon South Pole Stereographic projection (30121) coordinate system.

During the search for NAC images the target area was selected, and properly illuminated groups of images were identified according to orbit number groups. After rendering the selected NAC images, georeferencing was done to increase the accuracy of the image localization. Although substantial work has been done to improve the fitting of images, at several locations small errors can be found up to about 100 m distance. However these errors (misalignment of specific images) did not influence distance measurements as these were done using LOLA based data or was done only in one NAC image. The crater statistical analysis was also not influenced, carefully excluding the misalignment sections. Inventory of surface features mainly craters at different slope angle terrains were produced in order to see the occurrence of these features and related candidate formation processes (see Figs. 2 and 3).

Topographic measurements were done using gridded LOLA datasets with 40 m/pixel spatial resolution (Smith et al., 2010), downloaded from the website indicated at the end of references (LOLA data source). The accuracy of the distance and topographic measurements are characterized by slope accuracy in two directions ±1° using 10-m baseline,

Table 1
Parameters of the used NAC images. (Supporting Online Material).

Stamps	Incidence angle	North azimuth	Sub solar azimuth	Sub solar latitude	Sub solar longitude	Solar longitude
M171327852LC	88.62	359.64	91.58	−1.50	240.23	284.98
M171334640LC	88.59	359.90	91.49	−1.50	239.27	285.00
M171341429LC	88.60	359.78	91.40	−1.50	238.31	285.03
M171348217LC	88.57	0.10	91.30	−1.50	237.35	285.05
M171355005LC	88.61	359.64	91.20	−1.50	236.39	285.07
M171361792LC	88.57	0.03	91.10	−1.50	235.43	285.09
M171375367LC	88.53	0.56	90.89	−1.49	233.51	285.12
M171388944LC	88.55	0.36	90.68	−1.49	231.59	285.15
M171402519LC	88.50	0.89	90.48	−1.49	229.67	285.17
M171416097LC	88.52	0.65	90.27	−1.49	227.75	285.18
M171429673LC	88.48	1.09	90.07	−1.49	225.83	285.18
M171436462LC	88.46	1.24	89.97	−1.49	224.87	285.18
M171443250LC	88.45	1.44	89.88	−1.48	223.91	285.18
M171450038LC	88.45	1.41	89.78	−1.48	222.95	285.18
M171456826LC	88.45	1.43	89.69	−1.48	221.99	285.17
M171463614LC	88.44	1.51	89.60	−1.48	221.03	285.16
M171470402LC	88.41	1.84	89.50	−1.48	220.07	285.15
M171477190LC	88.45	1.32	89.41	−1.48	219.11	285.14
M171483978LC	88.44	1.48	89.32	−1.48	218.15	285.13
M171490766LC	88.45	1.45	89.22	−1.48	217.19	285.11
M171497555LC	88.46	1.22	89.13	−1.48	216.23	285.10
M171511130RC	88.44	182.52	91.33	−1.47	214.31	285.06
M171517918RC	88.46	183.30	91.24	−1.47	213.35	285.04
M171524705RC	88.45	182.83	91.16	−1.47	212.39	285.02
M171531493RC	88.50	184.45	91.08	−1.47	211.43	285.00
M171531493LC	88.50	0.69	88.70	−1.47	211.43	285.00

elevation precision ±0.1 m, radial accuracy <1 m, horizontal accuracy <50 m. The topographic data were used for elevation and slope angle determination, including statistical analysis of elevation values. As the ephemeris of LRO spacecraft is not as accurate as the LOLA measurements, thus the gridded DTMs contain linear artefacts, which are observable as small vertical (up to 1 m) and horizontal (typically up to 6 m) offsets. These lineaments are relatively dense in the polar region because of the polar orbit of LRO.

Some further **artefacts** have been recognized in the work. During the mosaicking of NAC images, some contacts between neighboring images remained visible as lines, because it was not possible to mosaic properly all parts of the images, as such multi-point adjusting (like rubber-sheet method) would have made up several gigabyte sized file, and cause the processing unrealistically slow. As a result along the contact between images some artefact lines could be identified, and occasionally some small surface features, especially craters could be duplicated rarely, however such situations were easily recognized and not considered during surface feature analysis, terrain classification and crater statistics. Because of the along track sampling of LOLA instrument there are linear features in the topographic dataset, which were ignored, and topographic profiles were selected on a way not to be influenced by such artefacts.

Identification of **boulders** was possible on NAC images with high resolution survey. There are some rock fields in de Gerlache crater, which could be easily separated from small impact craters based on the opposite arrangement of the illuminated and dark sides relatively to craters (which are depressions), and rocks might have much larger sized dark shadow than their solar illuminated bright part - opposite to craters.

Statistical **occurrence of impact craters** were also calculated and evaluated with ArcGIS and CraterStat software (Michael, 2021), which is well established for age estimation on the Moon (Orgel et al., 2018). For crater based age estimation large enough areas were used to locate at least 100 craters, and also lighting condition were favorable, no large dark and shadowed parts of the surfaced and no such large solar facing areas with oversaturated pixels were present that would have inhibited crater identification there. Those features were identified as craters on the images, which had a more solar illuminated (brighter) part and opposite to this a less illuminated (darker) area is present, and they form together a roughly circular shaped structure. Approaching the limit of spatial resolution of the images at 0.5 m, the firm identification is getting more difficult, thus craters smaller than 10 m were not counted. The aim was to improve the context to better understand regolith redistribution and mixing form recent craters in the shallow subsurface region. The occurrence of craters also helps to compare the effect of slope movements at different terrains. For the age estimation the new Neukum's chronology system and product function were used (Neukum et al., 2001) however at slopes the ages should be considered carefully as well as the occurrence of small craters and role of distant secondaries - see the related part in the Discussion section.

For **temperature analysis** based in the data from DIVINER instrument using infrared radiance at four broadband thermal channels were used, providing surface coverage, evaluating maximal and annual average values with spatial resolution around 0.5 km because of the high latitude location of the target area (Williams et al., 2019). The nadir-pointing Diviner RDR data from July, 5, 2009 to Feb 17, 2019 has been compiled into polar stereographic maps of temperatures poleward of 80° latitude at fixed local times and fixed subsolar longitudes, and provided an overview of diurnal temperatures. Temperature data were incorporated to ArcGIS and evaluated jointly with other datasets.

The **ice occurrence** data were implemented from different sources. The spectroscopic indication of water ice (280 m/pixel) was constrained by the M3 instrument (Li et al., 2018) on-board the Chandrayaan-1 mission. This instrument recorded the infrared absorption of water ice of surface radiation, providing 70 m spatial resolution on the average, indicating that water ice abundance increases toward the pole, up to about 500–750 ppm (Li and Milliken, 2017). Data also came also from the Lunar Orbiter Laser Altimeter (LOLA) analyzing the albedo calculated from the reflectivity at 1064.4 nm (Smith et al., 2010; Fisher et al., 2017; Qiao et al., 2019), providing latitude dependent spatial resolution, but at high latitude moderately homogeneous good resolution down to about 40 m was reached, consistent with occasionally 1–10% water ice occurrence on the surface. Another important data source is the Lyman Alpha Mapping Project (LAMP) (Gladstone et al., 2012; Hayne et al., 2015a, 2015b), evaluating FUV spectral reddening in the 164–173 nm region by water absorption with compared to the 175–190 nm region. This dataset provides 0.6° spatial resolution on the average, consistent with concentrated water ice occurrence of 1–2% in the PSRs area where the signal comes from the upper 100 nm thin surface layer.

Subsurface temperature modelling has been done according to King et al. (2020) using the Oxford 3D model for this target area, in order to estimate possible ice occurrence locations. The model includes a discrete subsurface exponential density profile, surface shadowing and scattering effects to simulate surface and subsurface temperatures across the Moon. For further technical details see the corresponding reference. Its horizontal spatial resolution was 128 px/degree, and vertically 25 layers were used in the top 2.5 m, providing 10 cm vertical resolution. The figures in this work represent the maximal temperature during a lunar day, e.g. an insolation cycle. During the evaluation water ice is assumed to be stable for long periods of time (>1 Gyr) if temperatures remain below 110 K on the surface (Schorghofer and Taylor, 2007), while in the subsurface at 0.5 m depth 125 K was considered as a limit.

All these datasets were jointly used and evaluated, where neutron spectrometry provides information on the top meter layer, LOLA and LAMP on the thin surface water ice using short wavelength reflection or emission, and M3 on the OH content of the top micrometer layer of the regolith. Linking these data to temperature values gives insight to the occurrence and expected long term stability of H_2O in the lunar regolith. Such information was evaluated together with various surface morphology of de Gerlache crater.

3. Results

For an overview of the target area it is worth to know the basic parameters: the **de Gerlache crater** is a 31 km diameter and roughly 7.5 km deep crater at about 30 km distance from the southern pole of the Moon. Much of the crater is in permanent shadow (Speyerer and Robinson, 2013). There is another, even deeper and somewhat younger crater superposing inside the southern part of the de Gerlache, which has steeper interior slope (often >30°), and its bottom surface is less tilted and less undulating (usually below 10° slope angle) than the observable bottom part of de Gerlache (with slopes below 20° and mostly below 15°), hereafter called "**large inner crater**". The highest parts of the da Gerlache rim is at the top and rightward (poleward) area in Fig. 1. The subunits (marked by A1, A2 … D4) were selected as examples for different terrain types, to survey the differences in smaller crater occurrence between them to see the characteristics of crater statistics based exposure age estimation. In Fig. 1. the probable ice occurrences are indicated by blue dots, where the albedo is consistent with ice occurrence using the Lyman-Alpha Mapping Project, which was later supported by the Lunar Orbiter Laser Altimeter and finally by the unique H_2O absorption from the Moon Mineralogy Mapper (M3) onboard India's Chandrayaan-1 mission.

3.1. Small scale surface morphology

The rationality of identifying and evaluating specific small surface features is to see the processes which were active and are currently active there, as these might modify the regolith, and possibly the occurrence of ice too. An overview of the various NAC images based surface features (craters, trench-like and girland features, boulders) with size scales of 10–100 m are indicated in Fig. 2. High resolution NAC image insets and also LOLA based topographic data are indicated in every second lines. Connecting these two datasets helps in the extrapolation for surface features that occur in the permanently shadowed areas, where no good optical images are available. Fig. 2 shows example 800 × 800 m sized insets of different surface types in different lines.

Detailed description of the selected surface feature types are

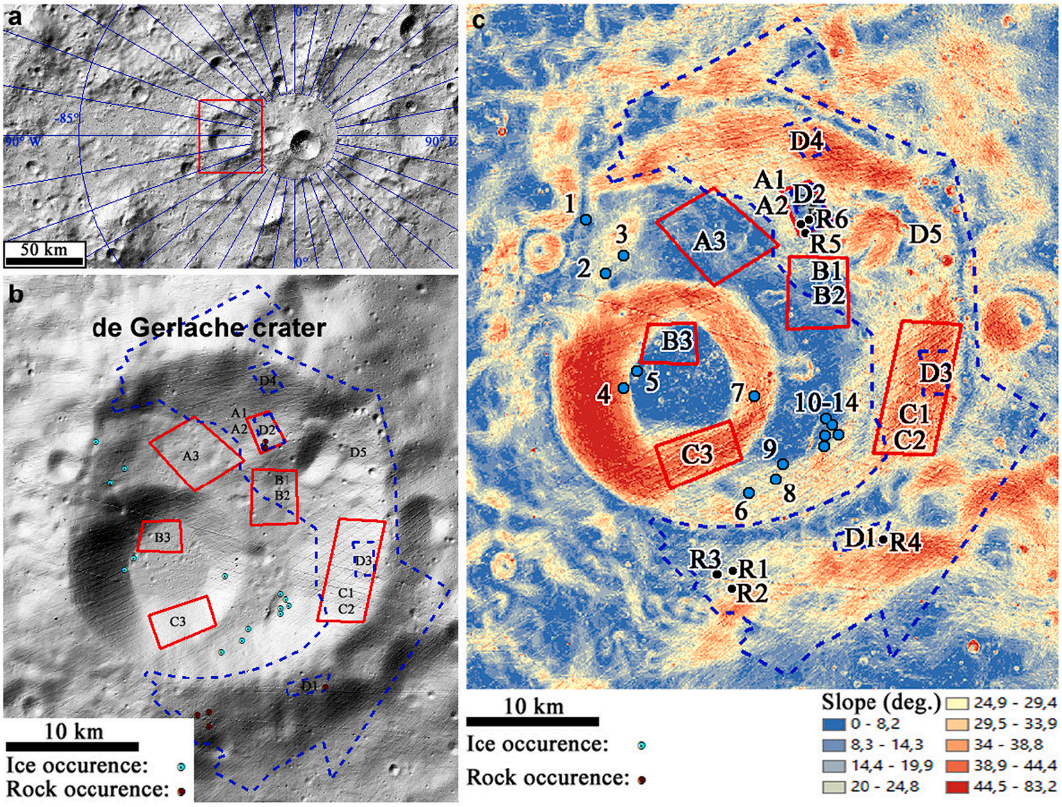

Fig. 1. Overview of the southern polar region of the Moon with the de Gerlache crater indicated (a panel), shaded topography map of the crater with the selected target units used in this work (b panel). Please note the smaller inner crater inside the larger de Gerlache. The slope map shows topography by color coding (c panel). The subunits used for detailed surface analysis, mainly for crater occurrence, which are outlined by red color, and marked by letters and numbers, while black dots with the letter "R" mark the identified rock groups. The small green dots with the black numbers mark potential ice occurrences based on Li et al. (2018). (For interpretation of the references to color in this figure legend, the reader is referred to the web version of this article.)

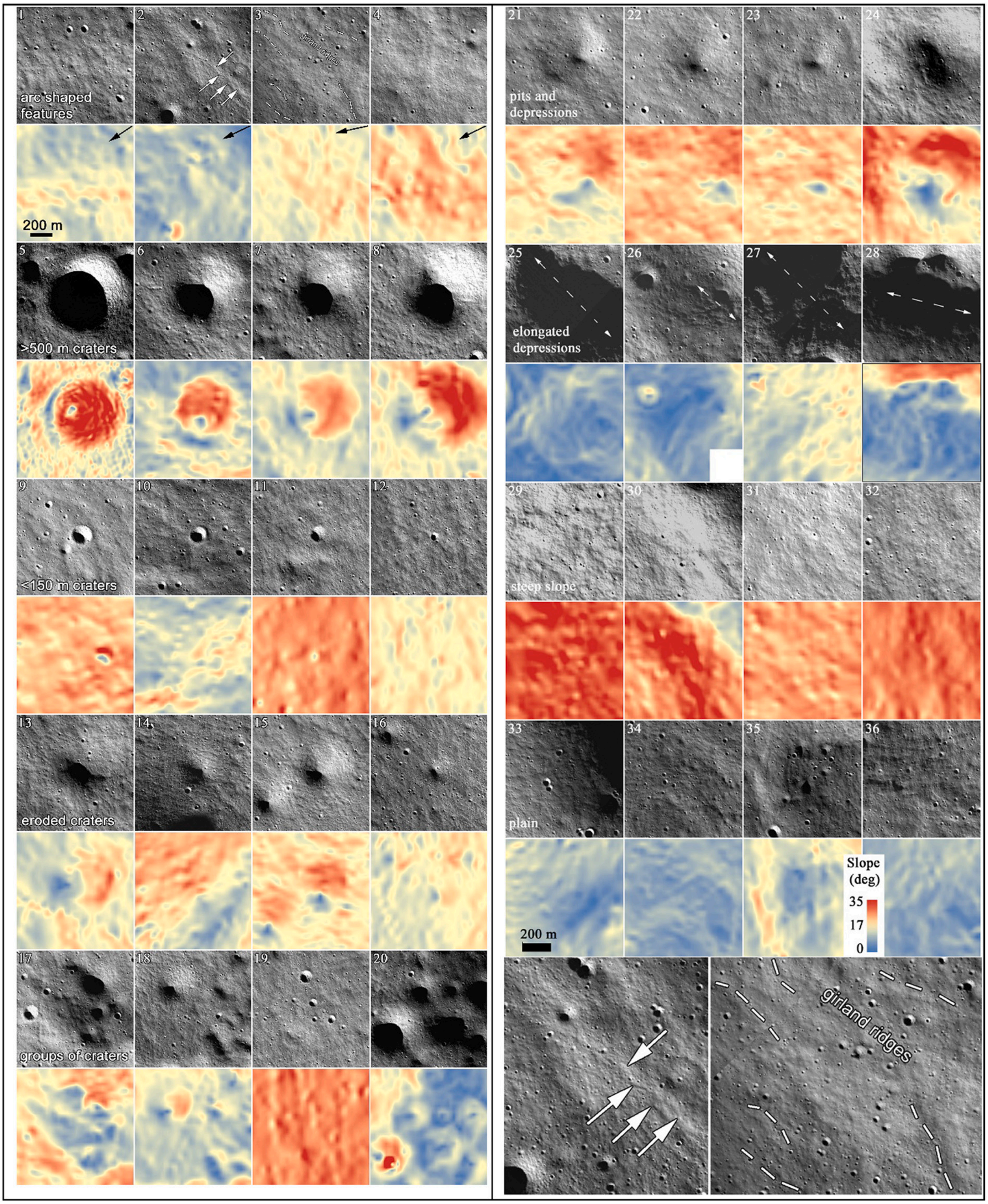

Fig. 2. Pairs of insets using NAC images (black and white) and slope angle maps (colorized panels every other lines) of the same small (800 × 800 m sized) area sections. For specific details see the corresponding text. In the first line black arrows mark the sloping direction. The dashed lines in 25–28 mark the elongated features. The 2 and 3 insets can be seen in magnified version at the bottom right. All these images were recorded at the better illuminated equator facing (e.g. poleward) areas of the de Gerlache crater. Please note the different spatial resolution of LOLA (40 m) and NAC (0.5 m) insets.

presented below (the numbers referring to the inset numbers, and two insets above each other marked with one number: the top inset shows the NAC image, the bottom one the corresponding part of the slope map):

- 1–4: Arc shaped features (later named girlands) with NW-SE (top left – lower right) direction on the surface, which could be identified as series of linear and curving shapes of brightness differences in visible images. They show a branching-like network, where several sections of them are present, occasionally meeting and merging but never crossing each other. These features are located in 100–200 m spacing from each other, and show roughly quasi-parallel arrangement. These brightness differences probably caused by the topographic undulations. The general slope direction of the panel is marked by black arrows at the top right corner with average slope angles of 1–11.6°, 2–8.8°, 3–14.3°, 4–16.5° respectively. Some girlands are marked by white arrows in panel 2, while the elongated direction of their ridges are marked by dashed lines in panel 3.

- 5–8: Large (about 450–1500 m diameter) craters at the center of the images (the first with 1:10000 scale, others with 1: 5000 scale), with a fresher one at left (5) and three older thus shallower craters (6, 7, 8) with smaller and differently shaped shadows by the smaller depth. Their depression could be firmly identified in the slope map panels, and their internal slope angles range up to 40° occasionally (red color). Artefact lines appear at the edge (from lower left to upper right) of the craters in the first two slope images. The rim is best observable in the inset number 5, while the insets 6–8 show more eroded craters with less pronounced rims.
- 9–12: Small craters (about 60–140 m diameter) at the center of the images with fresh elevated rim at 9 and 10 panels. These craters could not be identified on the slope map, as they are close to the about 40 m spatial resolution of topographic data. Artefact lines (running from lower left to upper right) influence the visibility of the craters in the slope images.
- 13–16: Heavily eroded craters at the center of the images, their diameters range between 200 and 500 m with shallow depression, covered by only a small part the self shadow. These craters have smaller totally shaded area in the same NAC images than the above listed craters (5–8 and 9–12 examples). Their depressions are barely visible in the slope map insets, although artefact lines are also there, but the depressions are not well outlined probably partly because of their eroded state.
- 17–20: Several craters close to each other, which make up an undulating terrain after some erosion. The first images show medium, the second elongated, the third small extended (artefact lines in the slope image) and the fourth large extended craters in the field of view.
- 21–24: Various pits and depressions with somewhat unusual shape at the center of the images may be remnants of old craters. Their depressions are barely visible in the slope maps, beside the artefact lines.
- 25–28: Elongated depressions, which might have formed by mass movements or crater degradation or both. Artefact lines appear in the first and third slope inset images.
- 29–32: Steep slope areas with >20°. Parallel and crossed artefact lines run through in the slope images.
- 33–36: Nearly plain, somewhat undulating surface, with <30° slope angle in all cases, and mostly <20°.

Although the majority of these surface feature types are well known from earlier lunar surface analyzing works (Agarwal et al., 2019; Hargitai and Kereszturi, 2015; Mahanti et al., 2018; Minton et al., 2019; Stopar et al., 2017; Wang et al., 2021), it is useful to see specifically which types are present here, how they look like, and among them a newly interpreted candidate is also present: the group of **quasi parallel arc shaped features**, called **girlands** hereafter (see Figs. 3 and 4). These features on the Moon make up such a pattern that resembles to those slope movement produced features, which are called girlands on the Earth, caused by slow creep-like movement on periglacial terrain slopes (Boltižiar, 2009; Lóczy et al., 2012). These were found in the Alps, composed of rocky debris arranged along specific pattern (Pécsi, 1961), and also identified in the Uludag mountain, where they appeared in a slope range of 2–40° (Türkeş and Zeynel, 2011). The term “garland” is also used equivalently in certain publications for resemble pattern at periglacial terrains in Ilgaz Mountain(Dede et al., 2012), Karçal (Lesser Caucasus Mts.), Kazdağ Mountains at high altitudes (Oliva et al., 2018), and periglacial areas of Mt. Esence (also known as Mt. Keşiş, Akkan and

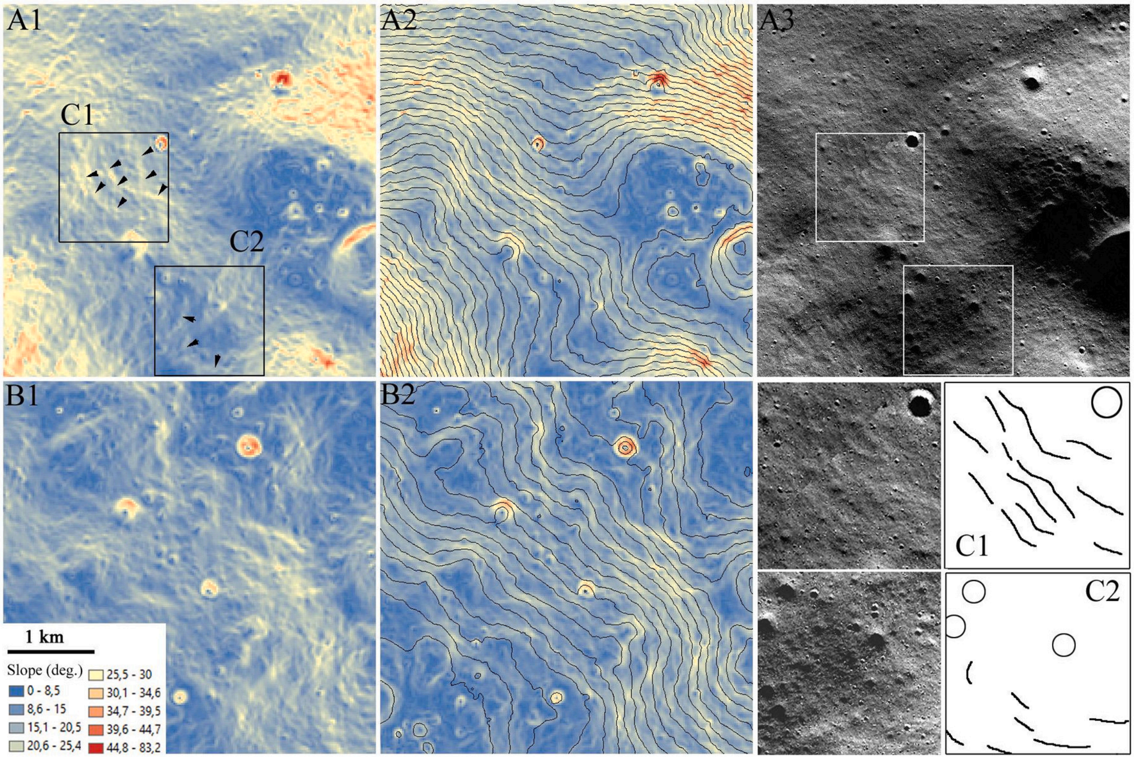

Fig. 3. Comparison of arc shaped girland groups in slope angle maps (1 and 2 columns) and their optical appearance in NAC image (3. column). A1: girlands in a solar illuminated area, A2: in solar illuminated area with contours, A3: NAC mosaic (images M169088184RC, M169094969RC, M169094969LC) in solar illuminated area. B1: in non illuminated area on slope map, B2: in non illuminated area with contour (black arrows mark the slope map based “fronts” of some girlands). C1 and C2 are magnified areas from A1 location and indicated as image at left and as graphical interpretation at right, where curved lines mark the crest of girlands.

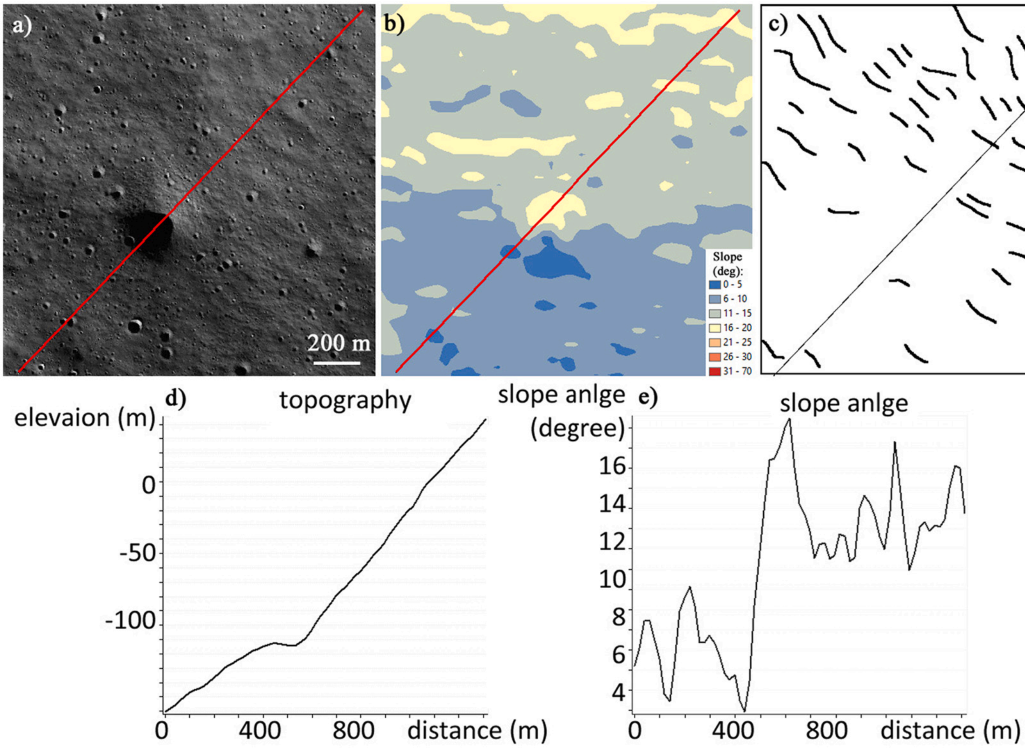

Fig. 4. Example image of girland occurrence and slope angle relation (M17140251LC). The inset (a) shows the NAC image with the profile, (b) inset shows the slope angle map, (c) the location of the most obvious girlands (interpretation), and (d) the shape of the topography where the profiles run the same direction in all panels e.g. from top right to lower left, while (e) inset shows the slope angle. It can be seen that the spatial density of girlands decrease substantially at low slope angle terrains below about 5–10°.

Tuncel, 1993). The formation of such girlands and garlands were attributed to seasonal frost actions (Çiçek et al., 2006) as micro-relief features at periglacial terrains (Kolčakovski, 1997). However we used this term here only because of the morphology and not formation reasons.

To better define these girland features, below a characterization is presented, while the relation to other already discussed features on literature based data presented in the Discussion section later. Fig. 3 shows examples for these girlands, which are quasi parallel, arc shaped ridge-like features, occurring on low slope angle areas with values around 5–15°, while the maximal slope angle at their frontal edge is between 10 and 12° usually. Further examples are visualized in Fig. 4. Topographic datasets with spatial resolution around 40 m is needed to identify their pattern, which is only available for polar terrains. The A1 and B1 insets show these ridges as they follow colored elongated curving lines, which form groups, and run almost parallel to each other at about 100 m distance scale. The features follow the contour lines of the topography (see A2 and B2 insets). At high resolution NAC images these features could be identified as topography influenced brightness features, with brighter part at the solar facing, and darker part at the antisolar facing direction. This observation is in agreement with the topography based ones: the curving lineaments are ridge-like topographic features, see examples in Fig. 4. However as they are low-slope angle features, could be obvious only on low insolation angle conditions, and high latitude terrains on the Moon are always recorded at such conditions.

At terrains below about 5° girlands are not or only barely present, while above about 20° degree they are also do not occur, instead slopeward elongated structures dominate from "strong" mass wasting at such steep locations. Fig. 4 demonstrates the relation of girland occurrence to slope angle, indicating that although the slope angles vary much at the used 40 m spatial resolution, trends can be identified. At the slope angle class below 10° (blue areas in inset b) the girlands show much smaller spatial density or they are absent there than above 10° (lower part of the inset), while girlands are obvious at the gray and yellow areas (top part, above about 10°). The change of slope angle along the profile that runs from the upper right to the lower left is visible between 10 and 18° in the girland rich area (left part of d and e insets).

Six example profiles roughly perpendicular to the arch shaped girland features at a low slope angle surface (<10°) unit can be seen in Fig. 5. The profiles 1–6 show the cross-sectional topography of different girland features, although the profiles number 4–7 might cross such a girland that could be considered one single continuous unit. However based on their appearance, girlands are somewhat "anastomosing"-like features, and it is difficult to identify exactly where one such girland terminates and a next one starts, even along the same direction. Beside the generally small slope angle of this terrain (top panel of the figure), the specific slope angle values at high spatial resolution varies, what is visualized along the red colored six profiles. The Sun illuminates the target area from the left, thus terrain sections sloping more to the left are brighter, while sections are less tilted toward the left are darker. The Sun was only 1.5° above the local horizon, and the area was tilted toward the left a bit, confirmed by LOLA profiles (see the profile sections in Fig. 5 bottom curves). The arc shaped girlands are poorly visible in the topographic profiles, investigating the middle of each panels (1–6), and despite the vertical exaggeration only small topographic undulations are visible as these are only gently sloping features. The expected variation in sloping is better visualized in the bottom of each panels, where the slope angle values are indicated. Here all values mean a sloping situation toward the left, however there are steeper and less steep parts, ranging between 4 and 5° and 10–12° at 40 m spatial resolution. Evaluating the top part of each panel (with a magnified part of NAC images), where profiles intersect bright (more solar facing) surface units, a local maximum in the slope angle is present (lower curve at each panel). These observations confirm that the arc shaped features are topographic step-like surface structures, where the more sunward tilted units are

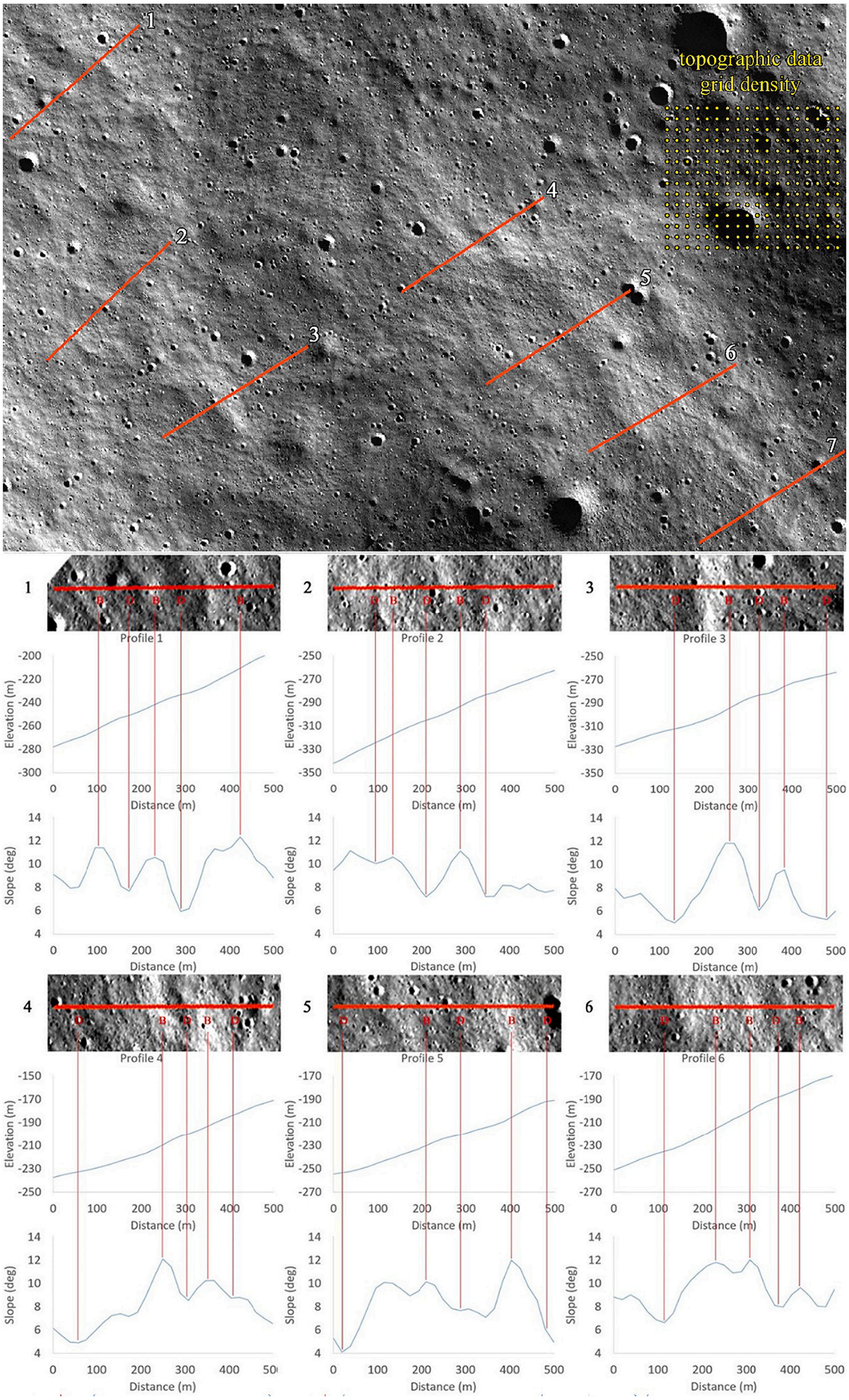

Fig. 5. The analyzed part of the mosaicked NAC M171416097lC, M171429673lC images (top) with the locations of the 6 profiles. Each profile is presented separately in the six insets (1–6) below, with the topography along the profile at the top (crossing each girland completely e.g. starting about 200 m from the given girland and terminating about 200 m from it in right angle to the direction of the given girland): the change of elevation (below in the middle) with 5-times vertical exaggeration, and the change of absolute slope angle values (bottom of each insets). At a small part of the top left image the spatial density of the used LOLA dataset was indicated to visualize the data grid density there.

brighter.

3.2. *Analysis of topography*

Topographic features are important not only because they might give further constraints on the formation of various surface units, but also as they influence the occurrence of shadows, what has a strong effect on the temperature and stability of surface ice. Below the general topographic surface properties are presented, excluding the above visualized arc shaped girland features, which have already been described. The maximal slope angle measured at the 40 m spatial resolution was 50° (excluding the linear artefacts) visualized in Fig. 6.

The slope map indicated in Fig. 7 with a color coded slope map demonstrates the general topographic characteristics in the area. The rim of the de Gerlache crater can be seen as a circular shaped moderately thin blue stripe, what shows $<10°$ slope angle areas (measured at 40 m spatial resolution). The most obvious feature is the inner crater with 17.9 km diameter and 2.8 km depth at the bottom left, superposing the bottom of the de Gerlache crater. It shows the steepest wall units up to about 66° slope angle (although at few locations, similarly steep slopes are present but with small areal occurrence, also connected to young craters). Five characteristic profiles are presented at the lower part of Fig. 7: 1–4 profiles show the southwest slope and bottom part of de Gerlache crater, while the profile no. 5 shows the smaller and younger craters' profile that superimposes the northeast part of the de Gerlache bottom plain. Most of the low slope angle areas are the bottom of de Gerlache and the large superposing crater, however small areas below bout 10° can be found at the lower part of the crater slope at the poleward part, and in a narrow ring-shaped occurrence the top rim of de Gerlache. Steep areas above 20° are almost solely occur at the slope of de Gerlache and the large superposing crater, while the steepest and homogeneous area of $>30°$ is present at the equatorward interior slope of the superposing crater. The interior wall of de Gerlache, especially at the poleward area shows somewhat hummocky appearance, indicating it is old and many subsequent impact events modified its appearance.

Evaluating the profiles, in about 1/3 of the total measured length the slope angle varies between 25° and 40° (marked with S in Fig. 7, the small inner crater's slope is represented by the profile 5 and the end of profile number 4. Low slope angle (P) units represent the bottom part of de Gerlache (1–4 profiles) and the bottom of the smaller inner crater (5 profile). The arc features (marked by A) are present in the low slope angle areas, while they are rare on steep slopes and plains too.

As it will be presented and discussed later (see Fig. 14 in Section 4.3), the most shadowed area is the poleward interior of the de Gerlache crater as expected, however there are some locations at the poleward part of the crater bottom, what receives limited illumination but still could retain ice in the shallow subsurface with low slope angle enough to fulfill engineering constrains for safe landing and surface operation. Slope angles are important aspects here, as most ice occurrences seem to be localized at moderately steep terrains here.

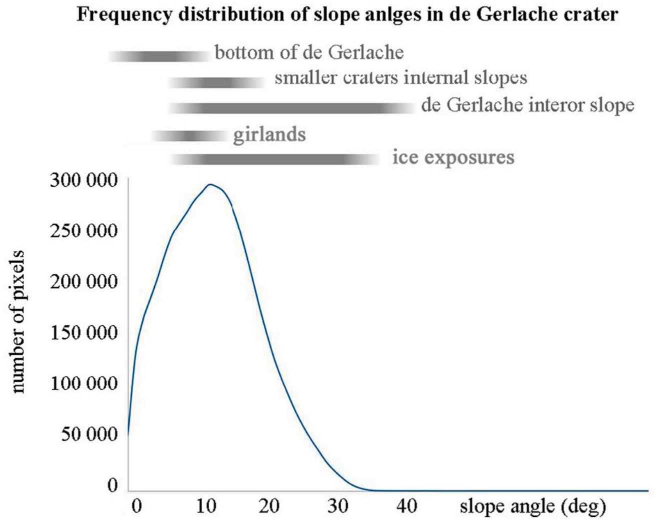

Fig. 6. Frequency distribution of slopes identified at 40 m spatial resolution using LOLA data. The most frequent slope values are in the 15–30° range. Main slope forming units are indicated by text at the top.

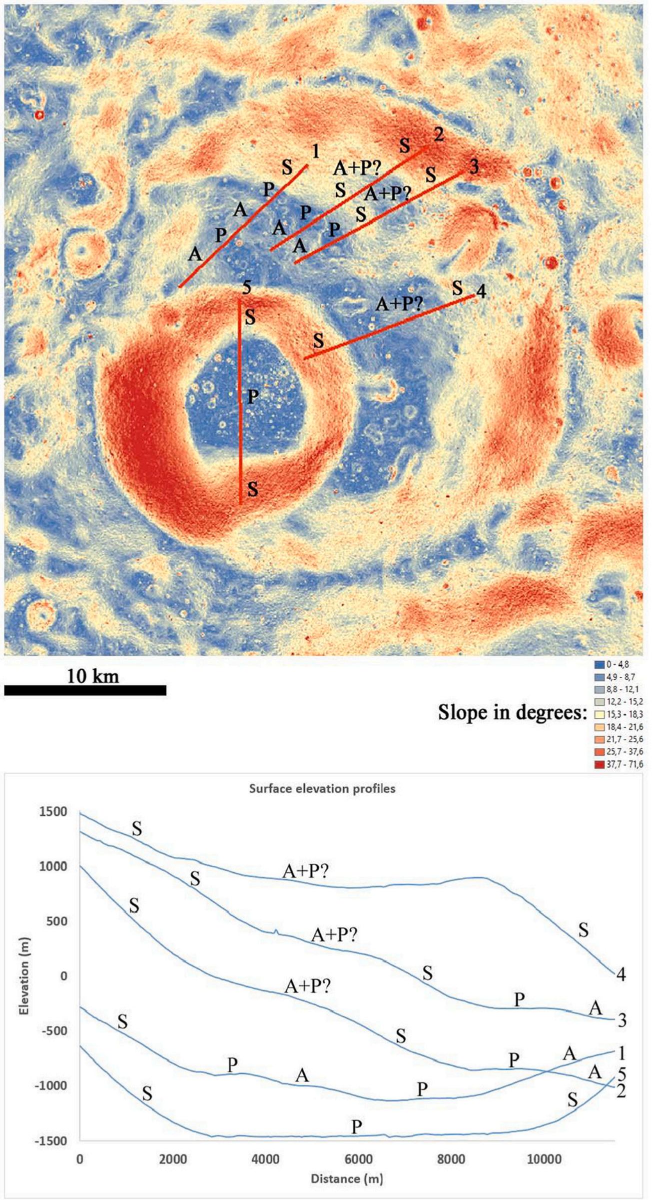

Fig. 7. Selected example profiles of 1–5 numbers. Locations can be seen above, while the topography along the profiles are visible below with 1.6-times vertical exaggeration. Acronyms characterize only roughly the slopes, where P is for plain (slope angle is below 4.2° at 200 m distance scale), S is for steep units, A is for the arc-shaped girland features hosting slopes, with generally occur at areas with slope angle between 5° and 15°.

3.3. *Crater analysis*

Craters show the "classical" appearance in the area of the de Gerlache crater. Fig. 8 shows examples for the diameter (horizontal axis) and depth (vertical axis) of relatively small craters (below 1 km diameter). Moderately good correlation can be seen according to the expectations, with having larger depth of the larger diameter craters, despite the data has 40 m horizontal spatial resolution, thus the values should have errors up to several percent, but the trend still exists. There is a wide range of crater depth values suggesting the existence of features with different degradation states, for example the 400–500 m diameter craters show a range of depth values between roughly 100 and 400 m. Impact craters and their degradation play a role in the regolith mixing, and gardening destroys these craters too, influencing the possible ice occurrence and stability there.

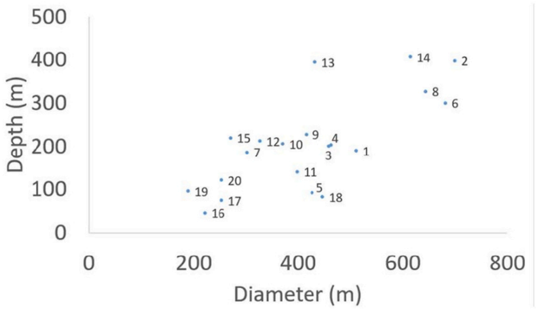

Fig. 8. Depth-diameter diagram of 20 craters in the illuminated area of NAC mosaic at the southern part of de Gerlache crater.

Examples of optical appearance and topography correlation can be seen in Fig. 9, where A1, B1, C1 panels show the optical based appearance of three selected areas and A2, B2 and C2 show their corresponding slope angle maps with the following average slope angle values for the given panels: A1 and A2: 7.2°, A3: 5.6°, B1and B2: 7.0°, B3: 5.4°, C1 and C2: 20.4°, C3: 22.2°. The A panels show examples of moderately smooth and plain areas with arc shaped features and $<10°$ slope angle. B insets show an arc poor, also moderately smooth and plain like area also with 10° slope angel on the average. C panels show sloping terrains with $>20°$ slope angle. While 1 and 2 panels show the solar illuminated areas, 3 panels (A3, B3, C3) show permanently shadowed units, where only topographic data is available.

The comparison demonstrates that craters and girland features make up many surface units in all regions, including the permanently shadowed ones too - e.g. if there have been solar illumination in the third insets, they would show probably the typical optical appearance what is visible in the first column. There are characteristic crater density values too: while in the moderately plain A and B rows elevated crater density can be observed, in the C row where the terrain is steep sloping, smaller crater density is relevant, there is a characteristic difference in the maximal size of craters too, probably as mass wasting dominates the surface and the lifetime of craters is much smaller. It is also visible that arc shaped girlands are missing from the steep slope angle areas. An artefact in the slope map of C2 panel is also visible, demonstrating the uncertainty and artefacts in the topographic data do not influence much the expected surface appearance in general.

3.4. Rock abundance

There are some rock fields in de Gerlache crater, see examples in Supplementary Table 1. The smallest firmly identified rock was about 5 m diameter, the largest 10 m diameter. Such rock populated areas are marked as R1-R6 in Fig. 10, which have about few 100 m diameter. The rock groups consist blocks of several dozen pieces. The group number R1, R2, R3, R5 are arranged around fresh looking craters; while R4 and R6 are located at a small (100–500 m sized) topographic elevation, probably these are bedrock outcrops.

Supplementary Table 1 SOM shows the six areas that consist of 10–100 rocks. The areal rock density values were calculated for an area of a polygon with the most distant rocks along the corners of the polygon. Please note that the highly elevated density values (several thousands at R3 and R5) came from only few (around a dozen) rocks scattered at small areas. The size of the identified rocks was smaller than 10 m in all cases.

3.5. Crater density based age analysis

Spatial crater occurrence was analyzed at 5 example areas, visualized in Fig. 11, their locations (marked with D1, D2, D3, D4, D5) in Fig. 1, and Table 2, to have insights to the characteristics of all mayor terrain types. The age of the whole de Gerlache crater was estimated by the age of the rim and the directly surrounding part of the ejecta blanket up to 50% of the crater diameter. The "low slope" area represents the interior, which probably was not influenced by slope movements. The "steep slope 1 and 2" areas are such terrains, where mass movements probably influenced the surface and ages might not be relevant. However the aim of using crater statistics is only to see the ratio of the spatial density of the same sized craters here.

Crater density values were analyzed only above 20 m diameter, where the crater identification was not influenced by the spatial resolution of the optical images. The reliability of the calculated age values are discussed later in the corresponding section, here only the numerical results are presented. During the analysis, no evident secondary crater group was identified, however the occurrence of distant secondaries could not be excluded. Several kink points were present in the SFD curves, indicating resurfacing events. Evaluating only the rim of de Gerlache, 1.9 Ga age was observable, and this value appeared in the above mentioned total age also, indicating a substantial part of the

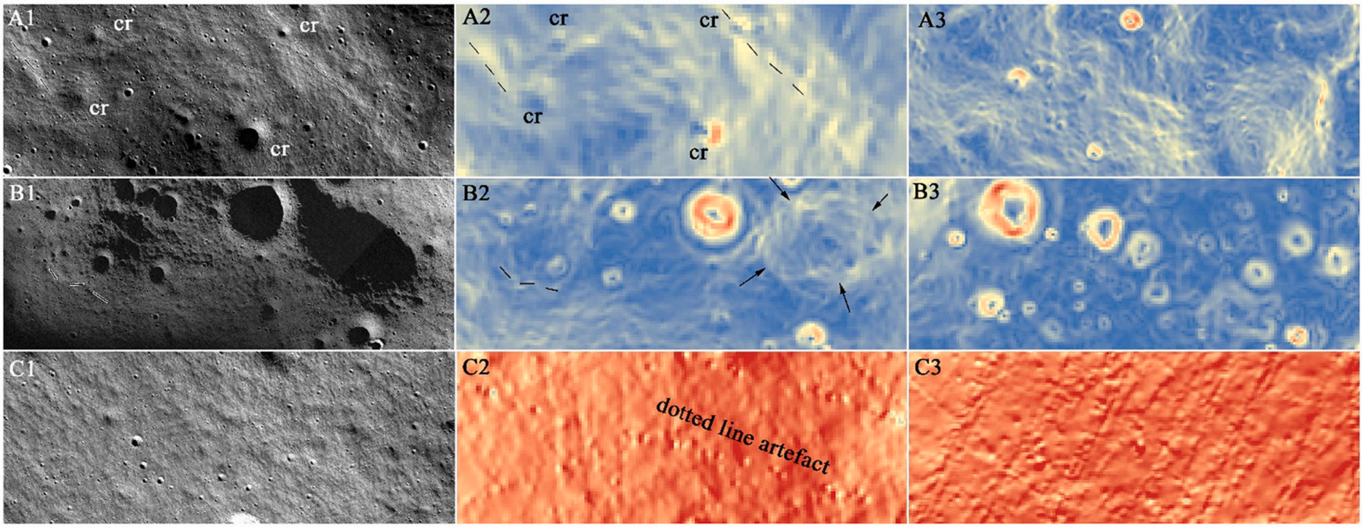

Fig. 9. Inset images of 3 km wide areas to compare the optical (1 column) and LOLA topography based slope angle (2 and 3 columns) of surface sections. A insets: Arc shaped girlands on a plain, two marked with dashed lines (A1: M171416097LC, M171429673LC NAC images). B: Cratered undulating plain, the dashed line of a girland feature (left), and topographic signature of concentric girlands at a circular depression (arrows in B2) (B1: M171443250LC, M171450038LC, M171456826LC images). C insets: slope area (C1:M171483978LC, M171490766LC, M171497555LC images). The 'cr' marks craters in A panels, panels' location can be seen in Fig. 1.

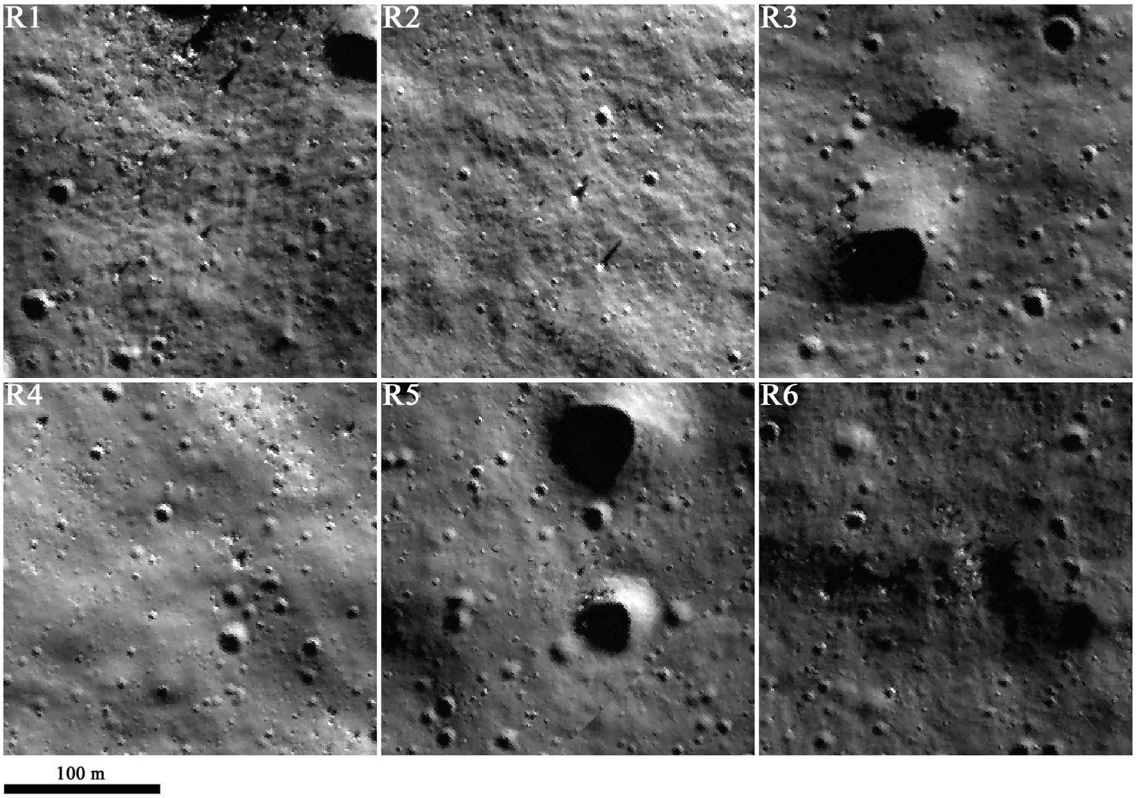

Fig. 10. Example images of rock groups in 250 × 250 m sized insets of NAC images. Panel numbers (R1, R2 etc.) are corresponding to the Supplementary Table 1. Please note that R4 and R6 are not visibly connected to craters but to small local elevations sized roughly equal to the width of the inset.

craters smaller than 400–500 m diameter have been erased around 1.9 Ga, possibly back falling of secondary ejecta blocks). Moderately old ages emerged at both sloping areas, 2.3 and 1.3 Ga, possibly also from the above mentioned possible "rejuvenation event".

3.6. Water ice occurrence

Neutron spectrometer based observations provide a rough estimation on the occurrence of H_2O in the top 1 m. Evaluating the LEND based measurements on-board LRO mission (Sanin et al., 2017), water-equivalent hydrogen (WEH) was estimated for the top regolith layer, what needs not necessarily indicate H_2O however it is improbable that other hydrogen bearing materials (like organics) provided the observed abundance. Unfortunately the spatial resolution of this data is low, and the size of the target de Gerlache crater is also relatively small, thus there is no worth of indicating WEH isoline on the maps of this work. The average WEH on this area was around 0.2 and 0.4 wt%, what is roughly the same as in the neighboring polar regions above 85°S, however the values might reach 0.5% occasionally. According to Elphic et al. (2007) in de Gerlache elevated WEH is characteristic, with values between 0.5 and 0.8 wt%, thus more elevated than in several nearby polar craters.

Evaluation of observations of M3, LOLA and LAMP identified some probable surface ice exposures in de Gerlache crater, indicated in Fig. 1 as small green dots, based on Li et al. (2018). The spatial resolution of these data is difficult to evaluate as different datasets were overlain and interpreted jointly (see Li et al., 2018). Thus these ice occurrences could be considered as possible separate but merged form identified small occurrences, with an uncertain diameter.

4. Discussion

In this section first the surface features are discussed in order to estimate the probable processes that happened there. Then the measured crater size frequency distribution based ages are evaluated, and the ice occurrence is discussed, while finally future mission relevant aspects are presented.

4.1. Evaluation of surface features' origin

Most of the observed surface morphological features in this paper are well known from other research works except the girlands. Large number of superposing craters were identified in de Gerlache, which showed a moderately wide range of values in diameter and depth parameters, suggesting crater erosion including impact gardening and crater degradation happened as it is expected in many cases. The crater density differed between the different slope angle areas, and showed smaller density at steeper slopes, possibly because of active slope processes and decreased crater stability there.

Beside the observed craters, **rock groups** could be identified, which came partly from fresh impact events and partly from exposed subsurface bedrock outcrops, both confirming active surface modification in the region. The expected lifetime of rocks blocks larger than about 2 m has 50% survival time of 40–60 Ma, 1–10% survival time of 150–300 Ma (Basilevsky et al., 2013). Based on these assumptions, considering that the observed maximal block size was below 10 m and the boulder field hosting craters could be around the scale or below 100 Ma old. As these craters are younger than the other same sized many craters without rock debris in the area, this fact indicates that the crater statistics based age estimation around 40–80 Ma might show a smaller value (and younger age) than the real exposure age there and could be caused by the so called equilibrium density, e.g. being an uncertain value.

An interesting group of features were identified by this work, the **slope girlands** (see examples earlier in Fig. 4, and for the characterization of resemble looking features on the Earth see Boltižiar, 2009 and Lóczy et al., 2012). As their elongated pattern follow the topographic

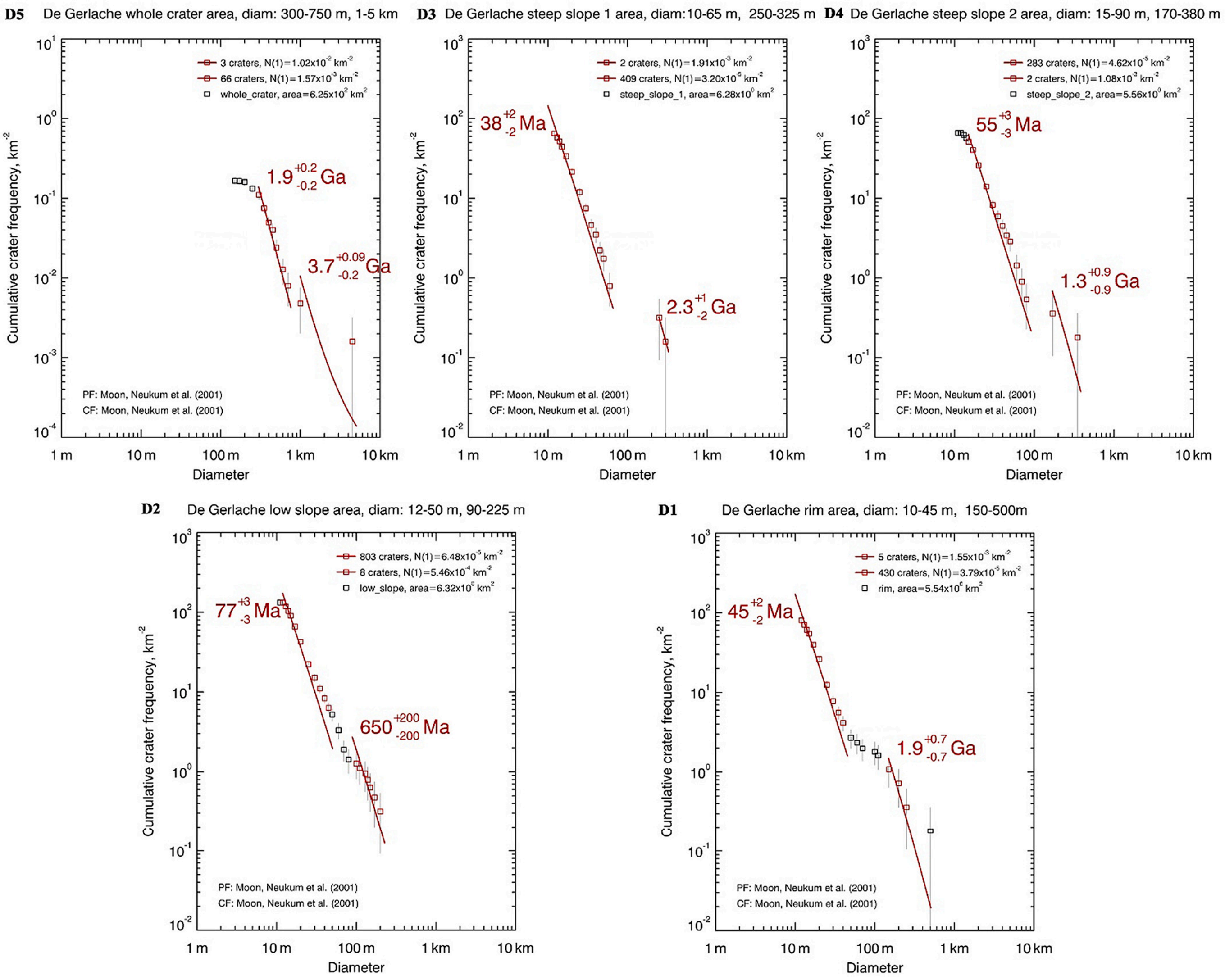

Fig. 11. Crater size frequency distribution curves for the analyzed terrains. At each terrain usually two ages were fitted, however even more could be indicated, but these two are the best established ones.

Table 2
Summary of the calculated crater size frequency distribution. Please note that age values for steep areas might not be realistic but used here only for comparison. The locations of D1, D2… can be seen in the Fig. 1.

Area id number	Area specification	Area (km2)	Slope angle (deg)	Crater number	Crater number diam >25 m km^{-2}	Crater density diam >25 m km^{-2}	min. diam (m)	Max. diam (m)	Younger age	Older age
D1	rim	5.54	14.1	445	69	12.44	12	530	45^{+2}_{-2}Ma	$1,9^{+0,7}_{-0,7}$Ga
D2	low slope	6.32	6.7	839	141	22.30	11	228	77^{+3}_{-3}Ma	650^{+200}_{-200}Ma
D3	steep slope1	6.28	23.5	411	75	11.94	12	332	38^{+2}_{-2}Ma	$2,3^{+1}_{-2}$Ga
D4	steep slope2	5.56	21.4	368	78	14.03	11	353	55^{+3}_{-3}Ma	$1,3^{+0,9}_{-0,9}$Ga
D5	whole crater	624.52	n.a.	104	n.a.	0.17	152	4762	$1,9^{+0,2}_{-0,2}$Ga	$3.7^{+0,1}_{-0,3}$Ga

isolines, and show an elevated frontal end in downward direction, they are probably formed by slope related mass movements. These slope girland features have been identified on topographic dataset for the first time, and outside the high spatial resolution LOLA track covered polar region (e.g. at lower latitude sites) such identification could be difficult because LOLA tracks are not dense enough there. These features partly resemble in appearance to slope girlands on the Earth, however on our planet plastic material plays a role in their formation, while similar is not expected on the Moon, because of the physical conditions there. The authors find very few related mentioning in the wide literature of mass movements on the Moon, what is understandable as high resolution images under low angle grazing insolation condition became available in large number only recently by LRO, and topographic data needed for their firm identification also became available only recently.

Earlier results on **mass movements** on the Moon were identified already in Apollo era images around 15 to 25 m spatial resolution (Pike, 1971), focused on steep crater interiors, large enough to provide visible details on images that show downslope bright or dark striae (Yangxiaoyi and Shevchenko, 2011), gully and channel-like structures from dry grain movement (Bart, 2007, Senthil Kumar et al., 2013). Granular avalanches were there producing slope oriented streaks (Kokelaar et al., 2017), and some mass movement features like some lunar landslides and boulder trails on the Moon could be triggered by fault motion (Weber et al., 2016) and impact driven shaking (Bickel et al., 2020). A range of mass movement features were analyzed by Xiao et al. (2013), evaluating falls, flows, slides, slumps, and creeps there. In this last work ripple shaped creep produced features (Fig. 5 in it), which they describe as slow movement produced flow-like features (Melosh, 2010) with convex upward smooth, rounded crests that run parallel to contour lines, caused by continuous downslope movement of regolith grains on the Moon (Lindsay, 1976) – probably are the same as what have been identified as girlands in this work. Many of the slope mass movement produced features are visible as exposed brighter subsurface locations with less effected regolith by space weathering. Such albedo differences are not visible at girlands, indicating even if they exposed subsurface units, such exposing process happened not recently.

Lunar slope movements were also evaluated using Circular Polarization Ratio observation together with crater statistics for the 1.7 km diameter Rozhdestvenskiy N polar crater (Pleascia, 2020), what indicates average retreat rate of 1 μm/year or 1 m/10 Ma, what is larger than the average regolith overturn (e.g., 5 cm in 10 Ma at Shorty Crater). Slope movement consequences was also confirmed by drill cores. Sample from the Apollo-16 and 17 cores indicated accretion of strongly irradiated surface material transported downslope at a rate of 1.5 cm/Ma (Evans et al., 1980), although this data might be uncertain and site specific. As these girland features emerge already around 4–6° slope angle, and do not show obvious downward striae pattern opposite to such mass movement which occur at steeper slopes, they might require other type of slope process. These slope angle values are substantially below the threshold limit of sand-like loose granular material, their formation probably requires some sudden energy input, like seismic shaking or ejecta falling by nearby impacts – however no evidence is available for these yet. The girlands might be specifically important at polar regions, where H_2O deposition could occur at cold traps including micro-scales, expose or bury it – the specific evaluation of this potential will be done in a future work. One further possibility to produce girland features is the creep mechanism, when the deformation happens in the plastic ice. This process requires specific temperature and substantial amount of bulk ice, what might not be present.

4.2. Evaluation of crater density and age values

Below the spatial density of small craters (which are not ideal for age estimation) were evaluated firstly, then the age relations are evaluated secondly, keeping in mind that age estimation using small craters or steep terrains are biased by and slope stability distant secondaries, thus crater lifetime is somewhat uncertain there. Comparison of the spatial density of small craters might point to regolith rejuvenation on the given terrain if there is a correlation of crater density and slope angle, what will be further explored in a future work.

The **shape of the crater size frequency distribution** curves indicates different size related densities relatively to the isochrones, what could be observed as kink points in the distribution. Such features are present at all curves, and indicated as a younger and as an older age values in the Table 2 separately. (For the locations of all counted craters see the Figure SOM.) The most relevant age for the formation of the de Gerlache crater indicate 4.1 Ga (marked as the “while crater” D5 unit), what coincides with the expectations that this crater formed around the Late Heavy Bombardment period. All curves showed a kink on them, thus at least two age domains could be identified.

Small **crater density** below 100 m diameter was evaluated at characteristic example locations from plain to steep slope areas. As expected, there is a correlation between the slope angle and the areal density of craters above 25 m diameter, having 22 crater/km^2 at 6.7°, and 12 crater/km^2 at 23.5°. Estimated exposure age values also showed this trend, ranging between 38 and 77 Ma. These moderately small values are based on the crater size domain below 50 m and are relevant for the shallow regolith where ice occurrence was evaluated. However for larger crater size domain relevant for deeper regolith, mainly above 100 m diameter, age values around 0.6–2.3 Ga are present, with less established by fewer craters at the surveyed areas.

It is difficult to evaluate recent surface ages considering craters smaller than 100 m, a kink in this size range can not be identified in every areas, and occasionally it is characteristic at smaller diameters, around 40–60 m. This younger age domain might represent an equilibrium population, thus need not necessarily be relevant to the exposure age of surfaces. The reduced crater density also indicates some moderately recent rejuvenation, what is natural at sloping terrains like this. Beside this uncertainty steeper slopes showed smaller crater density, what also influences the reliability of age estimation, but indicates recent mass movements and instability at the steeper slopes.

To see the relation between crater density and slope angle, the connection was evaluated for different subunits. Each of the D1, D2, D3 and D4 terrains were separated to three subunits according to three slope angle ranges: 0–12°, 12–24° and 24–36°, where the corresponding areas were selected at 40 m spatial resolution. Thus one indicated subunit contains all areas that fulfill the slope angle restrictions, irrespectively their location inside the given area or if they are continuous with each other. For example D1 12 contains all subunits of D1 which have slope angle below 12, even if these are made of small scattered patches.

There is a good correlation between the spatial density of craters >25 m sized and the average slope angle as it can be seen in Fig. 12 and also indicated in the Supplementary Table 2. At 25–30° slope angle the spatial density of craters is roughly half of the values as 5–10°, demonstrating smaller crater stability and/or stronger resurfacing at steeper slopes. The trend in the Fig. 12 and Supplementary Table 2 confirms the theoretical expectations that steeper slopes have poorer crater retention and/or stronger or more frequent rejuvenation. This finding is not influenced by observational effect toward the smaller sized craters, as the size limit of the used craters were 25 m here, and such craters could be firmly detected at all slope angle.

Supplementary Table 2 Supporting Online Material.

The spatial density of impact craters is influenced by several parameters, including exposure age, crater retention (by slope stability at steep terrains), contribution from secondary craters (especially in small diameter ranges, and for the Moon distant secondaries also). As these aspects influence various crater size ranges and various target area types differently, simple age estimations are not necessarily realistic in all cases. To avoid large uncertainties and possible misinterpretations, in the following the areal crater densities were compared and the inferred age values were considered only as a “secondary” tool to compare different target areas, and only for large craters was considered above about 100 m diameter, where the effect of slope movements and distant secondaries might be smaller.

Age estimation from large craters (diameter > 4.5 km) provided 3.7 Ga old for the whole de Gerache crater what is in agreement with the earlier work of Deutsch et al. (2020) who found 3.9 + 0.01–0.01 Ga. Evaluating craters smaller than 100 m, age values between 38 and 77 Ma were found at all surveyed terrain, what might show recent events, or especially some equilibrium population craters. Despite the error bars of these younger event age groups (3.5–3.7 Ga) do not overlap, because of the uncertainty of this crater occurrence based ages might show almost the same event of same age. Here the slope angle related limited lifetime might also contribute as a reason for this age domain. While the exposure age based values are uncertain, erosion gradually decreases the number of craters, and produces such shallow depressions finally that will not be considered and counted as craters.

4.3. Characteristics of ice bearing locations

Ice exposure locations (based on the joint evaluation of results from LAMP, LOLA and M3 instruments) were found at 14 locations in the de Gerlache crater, which are indicated in the Fig. 13 at high spatial

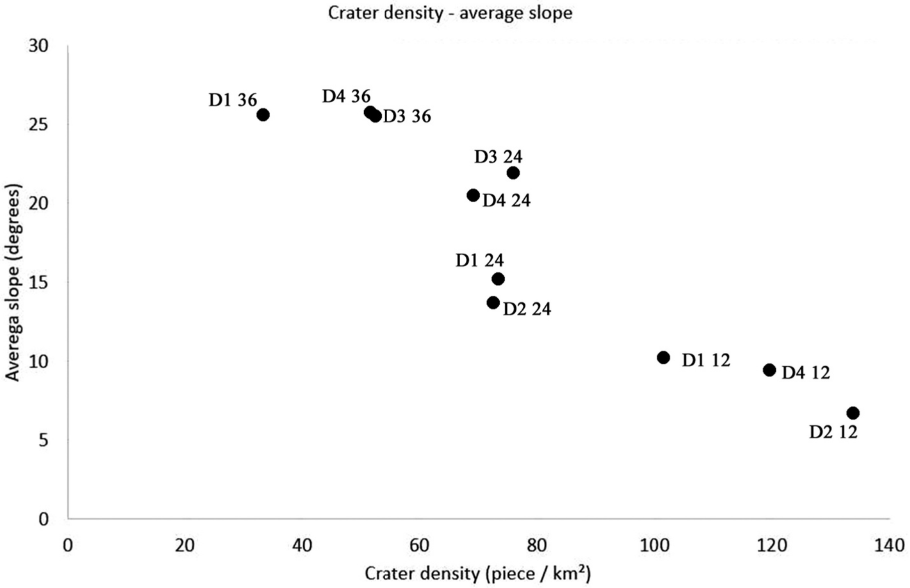

Fig. 12. Crater density values for the areas of different locations and slope angle values.

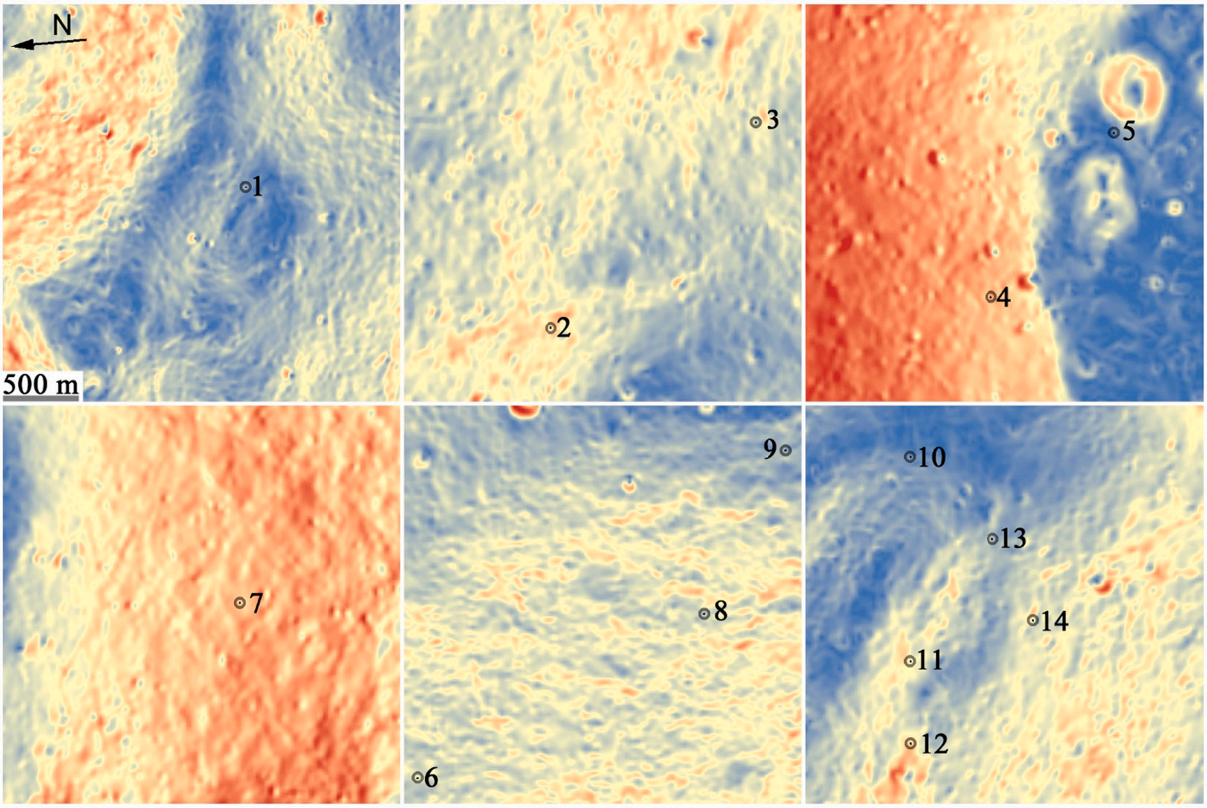

Fig. 13. Slope angle map based occurrences of the 14 exposed ice locations in de Gerlache crater. The small size of the small black dots are relevant for the footprint of LOLA laser spot, which were encircled by a partly transparent larger ring for better visualization.

resolution, marked with the numbers indicated in Fig. 1 before. As these are located in the PSR of de Gerlache, no optical image could be acquired of them, in the figure slope maps provide the background for visualization. The size of the small dots are the same as in reality, e.g. the size of the laser spot on the surface from the LOLA instrument around 40 m – however their exact real size is unknown, but a larger circle surrounding it is also indicated.

Based on these ice occurrence in Fig. 13 they are moderately sloping terrains (for numerical values see Table 3). Most ice occurrences are moderately steep slope angle areas, ranging between 6.7°-36.9° with an average of 21.6° supporting the earlier finding of Li and Milliken (2017) and Li et al., 2018. At the observed ice occurrence locations the summer average max. temperature was 103 K and ranged between 136 and 70 K, the min. temperature average was 38 K and ranged between 42 and 28 K. These results indicate that ice occurrence as observable exposures are visible in most cases (13 of 14 cases) with slope angle above 28°, in 7 of 7

Table 3
Basic parameters of the LOLA observations based exposed ice locations, including rough temperature values, and slope angles (this later was estimated by averaging a 100 m sized area's slope angles).

ID no.	Coordinates	Summer max. temp.	Winter max. temp	Summer min. temp. (K)	Winter min. temp. (K)	Slope angle (deg)
1	−81.44 -88.06	136.00	86.02	35.31	33.61	11.08
2	−85.17 -88.13	102.58	91.19	40.95	39.53	23.57
3	−83.60 -88.17	107.59	95.26	43.27	39.39	26.30
4	−93.79 -88.18	103.46	97.31	41.89	42.58	36.93
5	−92.67 -88.2	87.10	82.96	39.01	39.12	11.37
6	−104.12 -88.44	108.77	89.15	43.39	40.59	25.24
7	−95.29 -88.49	70.11	64.61	32.13	28.11	33.24
8	−103.34 -88.51	127.33	94.18	43.08	42.28	28.08
9	−102.09 -88.54	101.63	93.61	42.35	38.41	12.26
10	−98.35 -88.66	116.88	94.05	39.84	40.85	6.72
11	−100.3 -88.65	92.33	77.81	40.99	32.56	25.87
12	−101.08 -88.65	95.15	86.33	40.51	33.34	19.08
13	−99.26 -88.67	96.60	89.88	43.09	41.00	18.06
14	−100.12 -88.68	102.79	84.60	43.30	39.56	25.26
Average		103.45	87.64	40.65	37.92	21.65

cases above 35° and 6 of 14 cases above 30°. These values make probable that recent mass wasting could happen there, what is supported by their moderately reduced crater density (however because of possible equilibrium conditions exact age is not clear). Under such a situation slope movements could expose earlier deposited ice or work in dynamic equilibrium: bury H_2O and later expose it depending on the specific conditions.

No one of the ice exposure site is associated with observable craters, although only craters above about 100 m could be identified firmly without optical images. In theory if impacts expose ice here, the situation might be somewhat resembling to ice exposing young craters in the middle latitude zone of Mars (Dundas et al., 2021) – but in many aspects there are differences between the two environments. Roughly third of the locations are situated at probable areas of slope girlands, however these features could be difficult to identify at all areas, and even all ice exposures might occur on girlands covered areas. It is difficult to estimate the age of the slopes (here the age of the sallow, about 10 m thin top part of the regolith) as the crater retention time is much lower than in the case of nearly horizontal terrains. However the existence of the correlation between the slope angle and the spatial density of craters indicated in Fig. 13 above suggests these moderately steep slopes of ice exposures probably witnessed slope movement in the last some 10 Ma (this age is roughly the scale of crater based exposure age there, and no one crater is postponed by girlands, thus the smallest observable crater population is younger than the girlands).

Most of these locations are below 100 K temperature during all over the lunar day, allowing the existence of ice for extended duration on Ga time scale. However the maximal temperature is above the theoretically estimated 110 K for ice at 3 of 14 cases. This observation indicates that although the stable ice occurrence on Ga old scale with 110 K, but in shorter timescale surface ice might survive even only ephemerally illuminated locations. It is possible that the DIVINER based temperature values are not directly relevant for the exact and solely location of the ice exposure sites and averaging increases the values. As the footprint (spatial resolution) of DIVINER is much larger than LOLA, M3 and LAMP, it is also possible that LOLA hits a cold exposed location, but the DIVINER based temperature is relevant as an average of a larger area, including more solar exposed surfaces – thus the temperature at the ice might be lower than indicated above. It is important to note that a regional survey of several polar craters (Deutsch et al., 2000), including de Gerlache suggest close to surface ice is also can be found in moderately small (<15 km) diameter craters, indicating moderately recent ice accumulation or exposure there.

The above listed **slope angle** values are not far from the threshold angle of repose of lunar regolith. For dry sand ~34° is relevant (Carrier et al., 1991), and mass-wasting features on the Moon could remain observable for hundreds of millions of years because of the weak erosion (Kokelaar et al., 2017). (Although ice is there in the regolith, however it need not necessarily be a cementing agent.) These authors studied scars and deposits formed by mass wasting within four example craters at equatorial latitudes, with an influenced area about 1 km^2, and showed midslope angles ranged between 29° and 34° degrees. A survey of 20 km diameter craters by Wagner et al. (2013) suggests that slopes steeper than 36° are associated with blocky outcrops and not granular material, e.g. around 30° a threshold limit might exist for the stable existence of granular regolith. It is also possible that not "classical" mass movement events contribute in the exposure of subsurface ice, but smaller scale processes like **electrostatic dust levitation** of small dust grains (Colwell et al., 2007; Popel et al., 2013). Because of the complex electric potential at the polar region at many sharp shadows (Halekas et al., 2001), it is not clear how such dust related processes emerge in the permanently shadowed craters. In the polar craters the solar wind blowing above them creating a neutral plasma wake regions with few possibilities for electric grounding (Rhodes and Farrell, 2019), supporting charged conditions. LAMP observations provided an upper limit of the dust content of the lunar exosphere <10 grains cm^{-2} (0.1 μm grain radius) (Feldman et al., 2014), while it looks probable that nanoparticles in the lunar exosphere are modulated by impacts including meteor streams (Grava et al., 2017), and charging processes could influence the movement of such small nanoparticles effectively (Wooden et al., 2014).

The subsurface ice stability was estimated according to the modelled temperature of the top 2 m layer of the regolith. In the figures two temperature isolines are indicated for the surface ice stability about 110 K (threshold stability on Gy time scale, Schorghofer and Taylor, 2007), and for shallow subsurface ice stability at 1 m depth about 125 K. The areal distribution indicates that about half of the surface ice exposures are located inside the surface 110 K isotherm, but the other half is located at "warmer" areas – indicating these might be moderately young ice exposures. These locations in de Gerache crater are probably similar to those cold traps, what have been jointly evaluated several observations at many other locations on the Moon in general by Li et al. (2018), having at least 1000 ppm water-equivalent abundance. It is also worth to consider that the location of de Gerlache in larger context. Considering the paleopole position which were reconstructed from the inferred true polar wander of the Moon, the pole shift happened about at least 3.5 Ga ago (Siegler et al., 2016) – at this early period the de Gerlache was about 4 times farther from the ancient than the current pole, thus might be less ideal for early ice accumulation than periods after the polar wander.

4.4. Mission relevant aspects

Polar craters with PSRs are among the targets for next missions, thus it is worth considering de Gerlache in this aspects also. If a mission requires solar illumination during surface operation (especially with energy consuming activities like drilling and sampling), the equator facing slope of this crater could be the useful target, as it is occasionally illuminated, but large part of the time is in darkness, thus ice might accumulate there. However for radio contact with the Earth, a relay station might be needed on orbit as the Earth is rarely and barely visible from there. The observed slope movement signatures indicate that occasionally burial of surface deposited H_2O could happen or that buried ice could also be exposed. Considering the modelling based temperature distribution, part of this occasionally illuminated site has the modelled temperature below 125 K at 0.5 m depth, indicating possible occurrence of ice in the moderately shallow subsurface, accessible by a ~ 1 m deep drill in theory, like Luna-27 planned to do earlier (Heather et al., 2020).

Better targeting possibilities for next missions are present if operation is possible in the PSR, both in the bottom of the original de Gerlache and also inside the younger and inner superposing large crater formed at its bottom. Older craters might hold more ice (because accumulated there in the early periods by the more intensive bombardment, and also if we assume continuous accumulation). Direct ice exposures inferred from the joint existence of strong reflectance at 1064 nm and the low temperature are mostly situated at sloping terrains, as far as the spatial resolution of the datasets allow the analysis. The best occurrence of them to be reached by a mission, is a group of ice exposures, to the lower left part of the Fig. 14 image, around the edge of the de Gerlache bottom level.

Evaluating such solar illuminated locations, where shallow ice occurrence is realistic nearby to PSR, could provide optically guided landing, plus usage of solar power on the surface, and access by some mobile unit to nearby locations of possible surface exposed ice. Considering the densest probable surface ice occurrences including number 10–14 locations are still about 3 km from the occasionally illuminated equator facing slope, however its slope angle is usually above about 15°, thus probably too steep for safe landing. Closer to the ice occurrences, areas with few degrees of slopes are present, but this requires landing and operation in the dark. However it is worth mentioning that ice at the illuminated locations might be reachable within the top 1 m regolith layer (locations of this area are marked by orange arrows in 2b panel), what is achievable by drill systems being currently under development (Sefton-Nash et al., 2020) – although the slope angles allow only at limited locations the safe landing and operation. The potential areas with illumination, <1 m expected ice occurrence and about <10° for safe landing and surface operation are indicated by red color in Fig. 14 3b inset.

5. Conclusion

In this work the interesting but poorly analyzed de Gerlache crater with a permanent shadowed interior, located 30 km from the southern lunar pole was surveyed in order to see possible surface features related to water ice occurrence there. At its bottom a 15 km diameter superposing even deeper and younger crater can be also found beside many smaller overprinting craters. The model age based on crater size frequency distribution of the de Gerlache crater was found to be $3.7^{+0,\,1}_{-0,\,3}$Ga, formed around the late heavy bombardment. Different crater size domains represent different exposure age as expected: in the 100 m – 1 km size domain moderately early ages (roughly 1.3, 1.9, 2.3 Ga) emerged, which might represent a regional rejuvenation; while below 100 m crater size, at the different units resemble ages appeared between 38 and 77 Ma, possibly from recent equilibrium crater population – however this value is relevant for a shallow regolith layer only, but this is where H_2O content can be observed and analyzed.

Evaluating surface features beside the general ones, the so-called slope girlands are roughly few m high, ~100 m wide and few km long somewhat wave shaped quasi-parallel lineaments, running perpendicular to the sloping direction. These features might be similar to earlier

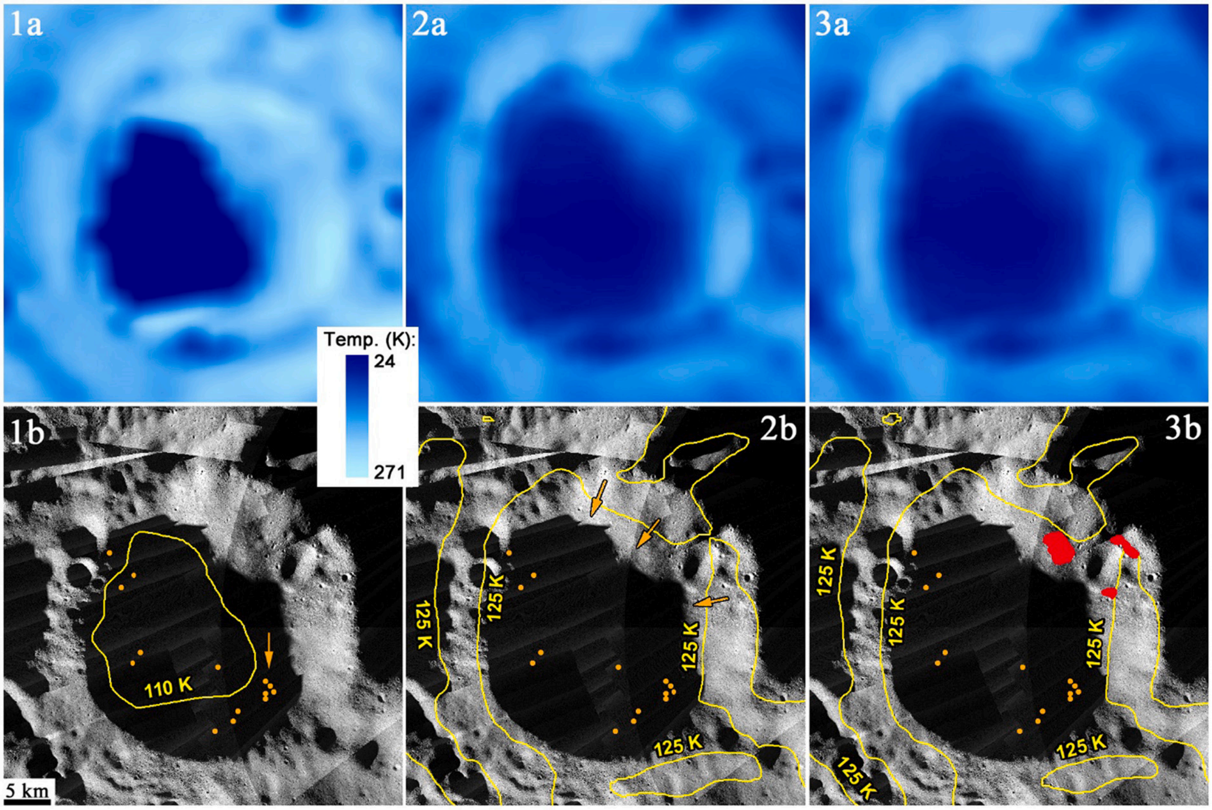

Fig. 14. Evaluation of temperature modelling. Top line: modelled temperature values at 1a: at the surface, 2a: at 0.5 m below the surface, 3a: at 1.0 m below the surface. Bottom line: two threshold isoline temperatures (110 K for surface 125 K for subsurface) overlain on a WAC mosaic for the surface (1b), 0.5 m depth (2b), and 1 m depth (3b). Orange dots mark surface ice exposures, and red areas in 3b inset mark sites with illumination plus <1 m expected ice occurrence and also <10° for safe landing and surface operation. (For interpretation of the references to color in this figure legend, the reader is referred to the web version of this article.)

identified creeping produces surface structures on the Moon, however this is their first identification at the polar region and using topographic dataset also, they might contribute in the burial or exposure of shallow subsurface ice. These features show a 10°-12° steep frontal edge facing toward the general downslope direction, indicating they are probably the result of slope movement. Such girlands occur down to 4–6° regional slope angle, and are overprinted by all craters, supposed not to be younger than around 50–100 Ma. The existence of girland-like features at only few angle steep slopes might require other than "classical" mass wasting processes observed at steep downward elongated striae pattern. These girlands might contribute in the exposure or burial of shallow subsurface ice. Beside these features, the spatial density of small recent craters (<25 m diameter) showed correlation with slope angle, also supporting the recent or ongoing slope changes. At 25–30° slope angle the spatial crater density is roughly half of the values at 5–10° because of stronger resurfacing at steeper slopes.

Most of the exposed ice occurrences were located on sloping units, with above 28° slope angle. No one of the ice exposure site is associated with observable craters, however craters below about 100 m might still be present there. As only half of them were located at areas with modelled surface temperature below 110 K, they might be long term unstable, but currently existing ice occurrences. This also requires moderately recent ice accumulation or exposure.

Regarding the mission relevant aspects, there was an area, where periodic solar illumination is available, while the subsurface temperature around 0.5 m and below is lower than 125 K, indicating potential long term preservation of ice there. This area might be useful for a targeted landing and drilling mission to reach ice in the future using solar power. Although important features have been identified in de Gerlache crater, several further questions emerged: could girland spacing indicate thickness of the upper loose regolith layer? Could their occurrence be connected to slope angle? And how could they support ice preservation at ideal locations? These issues require further work in the region.

Supplementary data to this article can be found online at https://doi.org/10.1016/j.icarus.2022.115231.

Declaration of Competing Interest

None.

Data availability

Data will be made available on request.

Acknowledgements

This work was supported by the POLICETECH project of ESA, funded by the KKM Űrkutatásért és Űrtevékenységért Felelős Főosztály Hungary. Contributions of the authors: Kereszturi A. coordinated the work and selected the target, Tomka R. made the GIS based work, Steinman V. contributed in the crater statistics based age estimation, Glaser P. the topographic data, Warren T. the thermodynamic calculation and Pal B. the implementation of thermodynamic data to GIS. No competing financial interests or other competing interests exist connected to the authors.

References

Agarwal, N., Haridas, A., Khanna, N., Srivastava, P., Jain, V., 2019. Study of morphology and degradation of lunar craters using Chandrayaan-1 data. Planet. Space Sci. 167, 42–53.

Akkan, E., Tuncel, M., 1993. Esence (Kesiş) Dağlarında Buzul Şekilleri, A.Ü. Coğrafyası Araştırma ve Uygulama Merkezi Dergisi 2, 225–240.

Arnold, J.R., 1979. Ice in the lunar polar regions. J. Geophys. Res. 84 (B10), 5659–5668. https://doi.org/10.1029/JB084iB10p05659.

Austin, A., Sherwood, B., Elliott, J., Colaprete, A., Zacny, K., Metzger, P., Sims, M., Schmitt, H., Magnus, S., Fong, T., Smith, M., Casillas, R.P., Howe, A.S., Voecks, G., Vaquero, M., Vendiola, V., 2020. Robotic lunar surface operations 2. Acta Astronaut. 176, 424–437.

Bart, G.D., 2007. Comparison of small lunar landslides and Martian gullies. Icarus 187, 417–421.

Basilevsky, A.T., Head, J.W., Horz, F., 2013. Survival times of meter-sized boulders on the surface of the moon. Planet. Space Sci. 89, 118–126.

Bickel, V.T., Aaron, J., Manconi, A., Loew, S., Mall, U., 2020. Impacts drive lunar rockfalls over billions of years. Nat. Commun. 11. Article number: 2862.

Boltižiar, M., 2009. The spatial patterns of the Tatra high-mountain landscape structure. Landform Anal. 10, 11–17.

Carrier, W.D., Olhoeft, G.R., Mendell, W., 1991. Physical properties of the lunar surface. In: Heiken, G., Vaniman, D., French, B.M. (Eds.), Lunar Sourcebook. Cambridge Univ. Press, New York, pp. 475–594.

Chabot, N.L., Ernst, C.M., Denevi, B.W., Nair, H., Murchie, S.L., Blewett, D.T., Head, J. W., Harmon, J.K., Solomon, S.C., 2013. Imaging inside Mercury's permanently shadowed craters: First images from MESSENGER. In: Lunar and Planetary Science Conference, 44 (Abstract 1693).

Chabot, N.L., Ernst, C.M., Denevi, B.W., Nair, H., Deutsch, A.N., Blewett, D.T., Murchie, S.L., Neumann, G.A., Mazarico, E., Paige, D.A., Harmon, J.K., Head, J.W., Solomon, S.C., 2014. Images of surface volatiles in Mercury's polar craters acquired by the MESSENGER spacecraft. Geology 42, 1051–1054.

Chabot, N.L., Shread, E.E., Harmon, J.K., 2018. Investigating Mercury's south polar deposits: Arecibo radar observations and high-resolution determination of illumination conditions. J. Geophys. Res. 123, 666–681.

Chin, G., Brylow, S., Foote, M., Garvin, J., Kasper, J., Keller, J., Litvak, M., Mitrofanov, I., Paige, D., Raney, K., Robinson, M., Sanin, A., Smith, D., Spence, H., Spudis, P., Stern, S.A., Zuber, M., 2007. Lunar reconnaissance orbiter overview: the instrument suite and mission. Space Sci. Rev. 129, 391–419.

Çiçek, İ., Gürgen, G., Tunçel, H., Doğu, A.F., 2006. Doğu Karadeniz dağları'nın glasyal morfolojisi. In: Proceedings of the Symposium of International Studies of the Mountainous Areas of Caucasus and Anatolia on Pleistocene and Today, pp. 28–42.

Cocks, F.H., Klenk, P.A., Watkins, S.A., Simmons, W.N., Cocks, J.C., Cocks, E.E., Sussingham, J.C., 2002. Lunar ice: adsorbed water on subsurface polar dust. Icarus 160, 386–397.

Colaprete, A., et al., 2010. Detection of water in the LCROSS ejecta plume. Science 463–468, 2010.

Colwell, J.E., Batiste, S., Horányi, M., Robertson, S., Sture, S., 2007. Lunar surface: dust dynamics and regolith mechanics. Rev. Geophys. 45, RG2006. https://doi.org/10.1029/2005RG000184.

Crawford, I., 2015. Lunar resources: A review. Prog. Phys. Geogr. 39 (2), 137–167.

Dede, V., Dengiz, O., Şeyda, B., Kuttusi, Z., 2012. The effect of temperature change due to elevation on soil properties in periglacial landforms in Ilgaz Mountains. Turkish J. Geogr. 78, 23–32.

Deutsch, H., Becker, K., Matt, S., Märk, T.D., 2000. Theoretical determination of absolute electron-impact ionization cross sections of molecules. Int. J. Mass Spectrom. 197, 37–69.

Deutsch, A.N., Head, J.W., Neumann, G.A., 2020. Analyzing the ages of south polar craters on the moon: implications for the sources and evolution of surface water ice. Icarus 336 (15), 113455.

D'Incecco, P., Helbert, J., D'Amore, M., Maturilli, A., Head, J.W., Klima, R.L., Izenberg, N.R., McClintock, W.E., Hiesinger, H., Ferrari, S., 2015. Shallow crustal composition of mercury as revealed by spectral properties and geological units of two impact craters. Planet. Space Sci. 119, 250–263.

Dundas, C.M., Mellon, M.T., Conway, S.J., Daubar, I.J., Williams, K.E., Ojha, L., Wray, J. J., Bramson, A.M., Byrne, S., McEwen, Alfred S., Posiolova, L.V., Speth, G., Donna, V., Landis, Margaret E., Morgan, Gareth A., Pathare, Asmin V., 2021. Widespread exposures of extensive clean shallow ice in the Midlatitudes of Mars. J. Geophys. Res. Planet 126 article id. e06617.

Elphic, R.C., Eke, V.R., Teodoro, L.F.A., Lawrence, D.J., Bussey, D.B.J., 2007. Models of the distribution and abundance of hydrogen at the lunar south pole. Geophys. Res. Lett. 34, L13204.

Evans, J.C., Fruchter, J.S., Reeves, J.H., Rancitelli, L.A., Perkins, R.W., 1980. Recent depositional history of Apollo 16 and 17 cores. In: 11th Lunar and Planetary Science Conference, Proceedings, 2, pp. 1497–1509 (A82-22296 09-91).

Fastook, J.L., Head, J.W., Deutsch, A.N., 2019. Glaciation on mercury: accumulation and flow of ice in permanently shadowed circum-polar crater interiors. Icarus 317, 81–93.

Feldman, P.D., Glenar, D.A., Stubbs, T.J., Retherford, K.D., Randall, G.G., Miles, P.F., Greathouse, T.K., Kaufmann, D.E., Parker, J.W., Alan Stern, S., 2014. Upper limits for a lunar dust exosphere from far-ultraviolet spectroscopy by LRO/LAMP. Icarus 233, 106–113.

Fisher, E.A., Lucey, P.-G., Lemelin, M., Greenhagen, B.T., Siegler, M.A., Mazarico, E., Aharonson, O., Williams, J.-P., Hayne, P.O., Neumann, G.A., Paige, D.A., Smith, D. E., Zuber, M.T., 2017. Evidence for surface water ice in the lunar polar regions using reflectance measurements from the lunar orbiter laser altimeter and temperature measurements from the diviner lunar radiometer experiment. Icarus 292, 74–85.

Gillmann, C., Golabek, G., Raymond, S., Tackley, P., Schonbachler, M., Dehant, V., Debaille, V., 2021. Late accretion and the origin of water on terrestrial planets in the solar system. In: EGU General Assembly, EGU21-5920.

Gladstone, G.R., Retherford, K.D., Egan, A.F., Kaufmann, D.E., Miles, P.F., Parker, J.W., Horvath, D., Rojas, P.M., Versteeg, M.H., Davis, M.W., Greathouse, T.K., Slater, D.C., Mukherjee, J., Steffl, A.J., Feldman, P.D., Hurley, D.M., Pryor, W.R., Hendrix, A.R., Mazarico, E., Stern, S.A., 2012. Far-ultraviolet reflectance properties of the Moon's permanently shadowed regions. J. Geophys. Res. 117 (E12).

Grant, J.A., Schultz, P.H., 1991. Gradational evolution of young, simple impact craters on the Earth. In: NASA, Washington, Reports of Planetary Geology and Geophysics Program 1990. xxx, pp. 152–153. SEE N92-10728 01-91.

Grava, C., Stubbs, T.J., Glenar, D.A., Retherford, K.D., 2017. LRO/LAMP campaign to detect a lunar nanodust exosphere. XLVIII. In: Lunar and Planetary Science, Abstract 2253.

Halekas, J.S., Mitchell, D.L., Lin, R.P., Frey, S., Hood, L.L., Acuña, M.H., Binder, A.B., 2001. Mapping of crustal magnetic anomalies on the lunar near side by the lunar prospector electron reflectometer. J. Geophys. Res. 106, 27,841–27,852.

Hargitai, H., Kereszturi, A. (Eds.), 2015. Encyclopaedia of Planetary Landforms. Springer, New York Heidelberg Dordrecht London.

Haruyama, J., Ohtake, M., Matsunaga, T., Morota, T., Honda, C., Yokota, Y., Pieters, C. M., Hara, S., Hioki, K., Saiki, K., Miyamoto, H., Iwasaki, A., Abe, M., Ogawa, Y., Takeda, H., Shirao, M., Yamaji, A., Josset, J.L., 2008. Lack of exposed ice inside lunar south pole Shackleton crater. Science 322 (5903), 938–939.

Hayne, P.O., Hendrix, A., Sefton-Nash, E., Siegler, M.A., Lucey, P.G., Retherford, K.D., Williams, J.-P., Greenhagen, B.T., Paige, D.A., 2015a. Evidence for exposed water ice in the Moon's south polar regions from lunar reconnaissance orbiter ultraviolet albedo and temperature measurements. Icarus 255, 58–69.

Hayne, P.O., Hendrix, A.R., Sefton-Nash, E., Siegler, M.A., Lucey, P.G., Retherford, K.D., et al., 2015b. Evidence for exposed water ice in the Moon's south polar regions from lunar reconnaissance orbiter ultraviolet albedo and temperature measurements. Icarus 255, 68–69.

Hayne, P.O., Aharonson, O., Schörghofer, 2021. Micro cold traps on the moon. Nat. Astronomy 5 (2), 1–7.

Head, J.W., Wilson, L., Deutsch, A.N., Rutherford, M.J., Saal, A.E., 2020. Volcanically induced transient atmospheres on the moon: assessment of duration, significance, and contributions to polar volatile traps. Geophys. Res. Lett. 47, GL089509.

Heather, D., Sefton-Nash, E., Fisackerly, R., Trautner, R., Barber, S., Reiss, P., Martin, D., Houdou, B., 2020. The ESA PROSPECT Payload for Luna27: Development Status. Europlanet Science Congress EPSC2020-672.

Humm, D.C., Tschimmel, M., Brylow, S.M., Mahanti, P., Tran, T.N., Braden, S.E., et al., 2016. Flight calibration of the LROC narrow angle camera. Space Sci. Rev. 200 (1–4), 431–473.

Jawin, E.R., Valencia, S.N., Watkins, R.N., Crowell, J.M., Neal, C.R., Schmidt, G., 2019. Lunar science for landed missions workshop findings report. Earth Space Sci. 6, 2–40.

King, O., Warren, T., Bowles, N., Sefton-Nash, E., Fisackerly, R., Trautner, R., 2020. The Oxford 3D thermophysical model with application to PROSPECT/Luna 27 study landing sites. Planet. Space Sci. 182, 104790.

Klumov, B.A., Berezhnoi, A.A., 2002. Possible origin of lunar ice. Adv. Space Res. 30, 1875–1881.

Kokelaar, B.P., Bahia, R.S., Joy, K.H., Viroulet, S., Gray, J.M.N.T., 2017. Granular avalanches on the moon: mass-wasting conditions, processes, and features. J. Geophys. Res. Planet 122 (9), 1893–1925.

Kolčakovski, D., 1997. Preliminary knowledge about the phenomena of girland soils (girland forms) of the high mountains in the republic of Macedonia. Macedonian J. Ecol. Environ. 5 (1), 41–48.

Li, S., Milliken, R., 2017. Water on the surface of the moon as seen by the moon mineralogy mapper: distribution, abundance, and origins. Sci. Adv. 3, e1701471.

Li, S., Lucey, Paul G., Milliken, R.E., Hayne, P.O., Fisher, E., Williams, J.-P., Hurley, D.M., Elphic, R.C., 2018. Direct evidence of surface exposed water ice in the lunar polar regions. Proc. Natl. Acad. Sci. 115 (36), 8907–8912.

Lindsay, J., 1976. Energy at the lunar surfaces. In: Kopal, Z., Cameron, A.G.W. (Eds.), Lunar Stratigraphy and Sedimentology, Developments in Solar System and Space Science, 3, pp. 45–55.

Lóczy, D., Stankoviansky, M., Kotarba, A., 2012. Recent Landform Evolution: The Carpatho-Balkan-Dinaric Region. Springer.

Mahanti, P., Robinson, M.S., Thompson, T.J., Henriksen, M.R., 2018. Small lunar craters at the Apollo 16 and 17 landing sites - morphology and degradation. Icarus 299, 475–501.

Mazarico, E., Neumann, G.A., Smith, D.E., Zuber, M.T., Torrence, M.H., 2011. Illumination conditions of the lunar polar regions using LOLA topography. Icarus 211, 1066–1081.

Melosh, H.J., 2010. Planetary Surface Processes. Cambridge University Press, Cambridge, UK.

Michael, G.G., 2021. Planetary Surface Dating with Craterstats3 — A New Open Source Implementation in Python. 2021 Annual Meeting of Planetary Geologic Mappers, Contribution No. 2610 id.7010.

Minton, D.A., Fassett, C.I., Hirabayashi, M., Howl, A., Richardson, J.E., 2019. The equilibrium size-frequency distribution of small craters reveals the effects of distal ejecta on lunar landscape morphology. Icarus 326, 63–87.

Mitrofanov, I.G., et al., 2010. Hydrogen mapping of the lunar south pole using the LRO neutron detector experiment LEND. Science 330, 483–486.

Needham, D.R., Kring, D.A., 2017. Lunar volcanism produced a transient atmosphere around the ancient moon. Earth Planet. Sci. Lett. 478, 175–178.

Neukum, G., Ivanov, B.A., Hartmann, W.K., 2001. Cratering records in the inner solar system in relation to the lunar reference system. Space Sci. Rev. 96, 55–86.

Neumann, G.A., et al., 2013. Bright and dark polar deposits on mercury: evidence for surface volatiles. Science 339, 296–300.

Oliva, M., Žebre, M., Guglielmin, M., Hughes, P.D., Çiner, A., Vieira, G., Bodin, X., Andrés, N., Colucci, R.R., García-hernández, C., Mora, C., Nofre, J., Palacios, D., Pérez-Alberti, A., Ribolini, A., Ruiz-fernández, J., Sarkaya, M.A., Serrano, E., Urdea, P., Yldrm, C., 2018. Permafrost conditions in the Mediterranean region since the last glaciation. Earth Sci. Rev. 185, 397–436.

Orgel, Cs, Michael, G., Fassett, C.I., van der Bogert, C.H., Riedel, C., Kneissl, T., Hiesinger, H., 2018. Ancient bombardment of the inner solar system: reinvestigation of the "fingerprints" of different impactor populations on the lunar surface. J. Geophys. Res. Planet 123, 748–762.

Paige, D.A., Siegler, M.A., Zhang, J.A., Hayne, P.O., Foote, E.J., Bennett, K.A., Vasavada, A.R., Greenhagen, B.T., Schofield, J.T., McCleese, D.J., Foote, M.C., 2010. Diviner lunar radiometer observations of cold traps in the moons south polar region. Science 330 (6003), 479–482.

Pécsi, M., 1961. A periglaciális talajfagyjelenségek főbb típusai Magyarországon. (in Hungarian language). Földr. Közi. 9 (85), 1–24, 1.

Pike, R.J., 1971. Some Preliminary Interpretations of Lunar Mass-Wasting Processes from Apollo 10 Photography. Analysis of Apollo 10 Photography and Visual Observations (Vols. NASA-SP-232). NASA Spec. Publ, Washington, D.C, pp. 14–20.

Pleascia, J.B., 2020. Permanently shadowed lunar north pole craters: Geology and implications for volatiles. In: 51st Lunar and Planetary Science Conference (abstract 2851).

Popel, S.I., Kopnin, S.I., Golub, A.P., Dol'nikov, G.G., Zakharov, A.V., Zelenyi, L.M., Izvekova, Y.N., 2013. Dusty plasma at the surface of the moon. Sol. Syst. Res. 47, 419–429.

Prem, P., Artemieva, N.A., Goldstein, D.B., Varghese, P.L., Trafton, L.M., 2015. Transport of water in a transient impact-generated lunar atmosphere. Icarus 255, 148–158.

Qiao, L., Ling, Z., Head, J.W., Ivanov, M.A., Liu, B., 2019. Analyses of lunar orbiter laser altimeter 1,064-nm albedo in permanently shadowed regions of polar crater flat floors: implications for surface water ice occurrence and future in situ exploration. Earth Planet. Sci. 6, 467–488.

Rhodes, R.J., Farrell, W.M., 2019. Drilling in a Lunar Polar Crater: Triboelectric Charge Regulation. Developing a New Space Economy 2019 (LPI Contrib. No. 2152) abstract 5119.

Sanin, A.B., Mitrofanov, I.G., Litvaka, M.L., Bakhtin, B.N., Bodnarik, J.B., Boynton, V., Chin, G., Evans, L.G., Harshman, K., Fedosov, F., Golovin, D.V., Kozyrev, A.V., Livengood, T.A., Malakhov, A.V., McClanahan, T.P., Mokrousov, M.I., Starr, R.D., Sagdeev, R.Z., Vostrukhin, A.A., 2017. Hydrogen distribution in the lunar polar regions. Icarus 283, 20–30.

Schorghofer, N., Taylor, G.J., 2007. Subsurface migration of H2O at lunar cold traps. J. Geophys. Res. 112 (E2).

Sefton-Nash, E., Fisackerly, R., Trautner, R., Barber, J.S., Reiss, P., Martin, D., Heather, D., Houdou, B., the PROSPECT Science Team and Industrial Consortium, 2020. The ESA PROSPECT payload for Luna 27: development status. In: 51st Lunar and Planetary Science Conference abstract 2367.

Senthil Kumar, P., Keerthi, V., Senthil Kumar, A., Mustard, John, Gopala Krishna, B., Amitabh, Ostrach, Lillian, R., Kring, David A., Kiran Kumar, A.S., Goswami, J.N., 2013. Gullies and landslides on the moon: evidence for dry-granular flows. J. Geophys. Res. Planet 118 (2), 206–223.

Shevchenko, V.V., 1999. On the cometary origin of the lunar ice. Sol. Syst. Res. 33, 400.

Siegler, M., Paige, D., Williams, J.P., Bills, B., 2015. Evolution of lunar polar ice stability. Icarus 255, 78–87.

Siegler, M.A., Miller, R.S., Keane, J.T., Laneuville, M., Paige, D.A., Matsuyama, I., Lawrence, D.J., Crotts, A., Poston, M.J., 2016. Lunar true polar wander inferred from polar hydrogen. Nature 531, 480–484.

Smith, David E., Zuber, Maria T., Jackson, Glenn B., Cavanaugh, John F., Neumann, Gregory A., Riris, Haris, Sun, Xiaoli, Zellar, Ronald S., Coltharp, Craig, Connelly, Joseph, Katz, Richard B., Kleyner, Igor, Liiva, Peter, Matuszeski, Adam, Mazarico, Erwan M., McGarry, Jan F., Novo-Gradac, Anne-Marie, Ott, Melanie N., Peters, Carlton, Ramos-Izquierdo, Luis A., Ramsey, Lawrence, Rowlands, David D., Schmidt, Stephen, Scott, V. Stanley, Shaw, George B., Smith, James C., Swinski, Joseph-Paul, Torrence, Mark H., Unger, Glenn, Yu, Anthony W., Zagwodzki, Thomas W., 2010. The lunar orbiter laser altimeter investigation on the lunar reconnaissance orbiter Mission. Space Sci. Rev. 150 (1–4), 209–241.

Speyerer, E.J., Robinson, M.S., 2013. Persistently illuminated regions at the lunar poles: ideal sites for future exploration. Icarus 222, 122–136.

Spudis, D.B.J., Butler, B., Carter, L., Chakraborty, M., Gillis-Davis, J., Goswami, J., Heggy, E., et al., 2010. Results of the mini-SAR imaging radar, Chandrayaan-1 mission to the moon. In: 41st Lunar and Planetary Science Conference abstract #1224.

Stacy, N.J.S., Campbell, D.B., Ford, P.G., 1997. Arecibo radar mapping of the lunar poles: A search for ice deposits. Science 276, 1527–1530.

Stopar, Julie D., Robinson, Mark S., Barnouin, Olivier S., McEwen, Alfred S., Speyerer, Emerson J., Henriksen, Megan R., Sutton, Sarah S., 2017. Relative depths of simple craters and the nature of the lunar regolith. Icarus 298, 34–48.

Tartèse, R., Sossi, P.A., Moynier, F., 2021. Conditions and extent of volatile loss from the moon during formation of the Procellarum basin. Proc. Natl. Acad. Sci. 118 id. 2023023118.

Teodoro, L., et al., 2014. How well do we know the polar hydrogen distribution. J. Geophys. Res. 574–593.

Tooley, C.R., Houghton, M.B., Saylor, R.S., Peddie, C., Everett, D.F., Baker, C.L., Safdie, K.N., 2010. Lunar reconnaissance orbiter mission and spacecraft design. Space Sci. Rev. 150, 23–62.

Trigo-Rodríguez, J.M., Mas-Sanz, E., Ibáñez-Insa, J., Alonso-Azcárate, J., 2020. Moon in-situ resources: clues from the study of Lunar achondrites in preparation for Artemis sample return missions. 14th Europlanet Science Congress 2020 id. EPSC2020-714.

Türkeş, M., Zeynel, Öztürk M., 2011. Garland and circle formations on Uludag. Turkish J. Geogr. Sci. 9 (2), 239–257.

Wagner, R.V., Robinson, M.S., Speyerer, E.J., Mahanti, P., 2013. Topography of 20-km diameter craters on the moon. In: 44th Lunar and Planetary Science Conference, Contribution No. 1719, p. 2924.

Wang, Yiran, Wu, Bo, Xue, Haiou, Li, Xiaoming, Ma, Jun, 2021. An improved global catalog of lunar impact craters (≥1 km) with 3D morphometric information and updates on global crater analysis. J. Geophys. Res. Planet 126 (9) article id. e06728.

Weber, R.C., Nahm, A.L., Yanites, B., Schmerr, N., 2016. Mass wasting on the Moon: Implications for seismicity. New Views of the Moon 2, Proceedings, LPI Contribution No. 1911 id.6009.

Williams, J.-P., Greenhagen, B.T., Paige, D.A., Schorghofer, N., Sefton-Nash, E., Hayne, P.O., Lucey, P.G., Siegler, M.A., Aye, K.M., 2019. Seasonal polar temperatures on the moon. J. Geophys. Res. 124, 2505–2521.

Wooden, D.H., Colaprete, A., Cook, A.M., Shirley, M.H., Vargo, K.E., Elphic, R.C., Stubbs, T.J., Glenar, D.A., 2014. LADEE UVS Observations of Atoms and Dust in the Lunar Tail. American Astronomical Society. DPS meeting #46, id.306.02.

Xiao, Z., Zeng, Z., Ding, N., Molaro, J., 2013. Mass wasting features on the moon—how active is the lunar surface? Earth Planet. Sci. Lett. 376, 1–11.

Yangxiaoyi, L., Shevchenko, V.V., 2011. Dry debris flow on the moon: Chang'e – 2 data. In: 42nd Lunar and Planetary Science Conference abstract 1254.

Zhu, C., Gillis-Davis, J.J., Crandall, P.B., Ishii, H.A., Bradley, J.P., Corley, L.M., Kaiser, R. I., 2019. Untangling the formation and liberation of water in the lunar regolith. Proc. Natl. Acad. Sci. 116 (23), 11165–11170.

Zuber, M., Head, J., Smith, D., Neumann, G.A., Mazarico, E., Torrence, M.H., Aharonson, O., Tye, A.R., Fassett, C.I., Rosenburg, M.A., Melosh, H.J., 2012. Constraints on the volatile distribution within Shackleton crater at the lunar south pole. Nature 486, 378–381.